Early stages of agglomeration of adhesive particles in fully-developed turbulent pipe flows

Hærvig, Jakob; Sørensen, Kim; Condra, Thomas Joseph

Published in:
International Journal of Multiphase Flow

DOI (link to publication from Publisher):
10.1016/j.ijmultiphaseflow.2018.04.017

Publication date:
2018

Document Version
Accepted author manuscript, peer reviewed version

Citation for published version (APA):
Hærvig, J., Sørensen, K., & Condra, T. J. (2018). Early stages of agglomeration of adhesive particles in fully-developed turbulent pipe flows. *International Journal of Multiphase Flow*, *106*, 254-267. https://doi.org/10.1016/j.ijmultiphaseflow.2018.04.017

Early Stages of Agglomeration of Adhesive Particles in Fully-Developed Turbulent Pipe Flows

J. Hærvig[a,*], K. Sørensen[a], T.J. Condra[a]

[a] *Aalborg University, Department of Energy Technology, Pontoppidanstræde 111, DK-9220 Aalborg, Denmark*

Abstract

We study how changes in particle response time and adhesiveness affect how particles agglomeration in fully-developed turbulent pipe flows. For this purpose, particle-particle and particle-wall interactions are fully-resolved using the soft-sphere Discrete Element Method (DEM) modified to include adhesiveness due to van der Waals forces and electrostatic forces through JKR theory. The particulate phase is two-way coupled to the turbulent fluid phase, which is partly resolved using Large Eddy Simulations (LES). First, we validate the simulations by grid refinement and by comparing the statistics of the flow field to experiments in literature. Secondly, we vary the particle response time $\tau_\mathrm{p} = \rho_\mathrm{p} d_\mathrm{p}^2/(18\mu)$ and observe the largest agglomerates in terms of average number of particles per agglomerate to be formed by primary particles with intermediate Stokes numbers, e.g. $\mathrm{St_e} = \tau_\mathrm{p}/\tau_\mathrm{e} \approx 6.4$ where $\tau_\mathrm{e} = D/U$ is the eddy turn over time or $\mathrm{St}_\mathcal{L} = \tau_\mathrm{p}/\tau_\mathcal{L} \approx 46.4$ in terms of the integral time scale of the turbulent flow $\tau_\mathcal{L}$. Then we show how the total fraction of particles contained in agglomerates is almost constant up to $\mathrm{St_e} = 6.4$ after which there is a sudden drop in the fraction of particles contained in agglomerates. To investigate the transition from non-adhesive particles to highly adhesive particles, we vary the adhesiveness parameter $\mathrm{Ad} = \gamma/(\rho_\mathrm{p} U^2 d_\mathrm{p})$ to obtain two extremes; one with weakly adhesive particles where less than 3 % of particles are contained in agglomerates to highly adhesive particles where more than 70 % are contained in agglomerates. While varying the adhesiveness of the primary particles for a fixed particle response time, we observe three distinct regimes. For almost non-adhesive particles, the agglomerate number density is highest towards the centre of the pipe with a maximum at $0.2 < r/R < 0.3$. Slightly more adhesive particles form a almost uniform agglomerate number density profile while for highly adhesive particles there is a distinct peak in agglomerate number density at the wall where particles and agglomerates deposit.

Keywords: Adhesive particles, Agglomeration, Turbulent pipe flow, Large Eddy Simulation (LES), Soft-sphere Discrete Element Method (DEM), Johnson-Kendall-Roberts (JKR) model

1. Introduction

The transport, agglomeration and subsequently deposition of small adhesive particles play important roles in many industrial and fundamental processes. These processes range from particles accumulating at heat transfer surfaces, particles blocking pores in membrane filtration systems, particles being inhaled and deposited in our lungs to interstellar medium agglomerating causing early stages of new planets to form in space.

All agglomeration and deposition processes are a result of particles colliding with one another or a wall. The mechanisms governing particle collisions of non-adhesive particles in turbulent flows have been devoted much attention in literature. These studies date back to Saffman and Turner [1] who investigated the collision frequency in isotropic turbulent flows in the limiting case of finite size tracer particles with response times much smaller than fluid response time $\tau_\mathrm{p} \ll \tau_\mathrm{f}$ and Abrahamson [2] who investigated the collision frequency in the other limiting case of heavy particles with $\tau_\mathrm{p} \gg \tau_\mathrm{f}$. For particles having $\tau_\mathrm{p} \approx \tau_\mathrm{f}$, various correlations have been proposed in literate [3]. However, as particles begin to adhere to one another and the turbulent flow of interest is anisotropic, e.g. a pipe flow, a common approach is to resolve only the turbulence scales that affect motion of the particles considered using LES. Due to the wide range of applications where particles are transported by a turbulent gaseous flow, a lot of research has been carried out [4]. As noted in several studies including Squires and Eaton [5], Eaton and Fessler [6], particles heavier than the fluid with response time similar to that of the local fluid flow are commonly observed to preferentially collect in regions with low vorticity and high strain rate in turbulent flows. This is most pronounced for particles with response time similar to that of the local turbulent flow. Furthermore, there is evidence that particles in an anisotropic turbulent flow tend to accumulate in regions with lower turbulence [7] due to turbophoresis. Based on a collection of experimental data from literature reporting

*Corresponding author: Tel.: +45 22 50 81 31
Email address: jah@et.aau.dk (J. Hærvig)

particle transport in turbulent pipe flows, Rao [8] suggest that the motion of particles with $\mathrm{St_e} < 5$ is dominated by viscous forces and generally follow fluid streamlines closely. At intermediate Stokes numbers $5 < \mathrm{St_e} < 40$ the motion of particles is partly correlated with local turbulence causing a high collision rate. At sufficiently high Stokes numbers $\mathrm{St_e} > 40$ particles tend to follow the mean flow while being less affected by local turbulence structures in the flow, which results in a low collision rate.

Different approaches exist to model the agglomeration process. One approach is to represent agglomerates by equivalent spheres that grow in size as the number of particles contained in the agglomerate increase [9, 10]. However, as shown by Brasil et al. [11], the morphology of agglomerates differs significantly depending on how the agglomerates are formed, the properties of the primary particles and properties of the fluid flow surrounding the particles. Based on the Euler-Lagrangian approach, Sommerfeld and Stübing [12] proposed a computational efficient agglomerate structure model. Using this model, agglomerates are treated as point particles that carry additional information such as locations of the primary particles and binding forces holding the agglomerates together. Based on these properties, parameters such as the convex hull and fractal dimension can be calculated and used to relate agglomerate structure to flow resistance coefficients.

Another approach is to track every particle but assume the particles to stay adhered when agglomerated or deposited on a wall. However, the DEM study of laminar channel flow by Marshall [13] shows that phenomena such as bending and break-off of agglomerates occur frequently and play important roles to accurately predict the state where the rate of particles being re-entrained back into the fluid asymptotically approaches the rate of particles being deposited. Furthermore, the study suggests the mechanism of agglomerates continuously breaking up as agglomerates are formed to be controlled by impacting particles or agglomerates rather that fluid forces.

As noted in most studies coupling DEM to a fluid phase, there is typically a large difference between the time step sizes required to resolve particle collisions δt_{DEM} and fluid flows δt_{f}, so that $\delta t_{\mathrm{col}} \ll \delta t_{\mathrm{f}}$. As $\delta t_{\mathrm{col}} = \mathcal{O}(10^{-9}\ \mathrm{s})$, this is also valid for a wide range of turbulent flows. This fact is commonly used to speed up coupled simulations by introducing softer particles by lowering the particle stiffness and thereby making particle collisions take place over longer time periods. However, as noted in studies by Kobayashi et al. [14], Gu et al. [15], Hærvig et al. [16], depending on the adhesiveness model, introducing softer particles should be accompanied by a lower adhesive forces in order for the collision outcome (stick/rebound) to stay the same.

When the agglomerates increase in size, the study by Dizaji and Marshall [17] shows that the local fluid velocity in an agglomerate becomes increasingly correlated with the agglomerate velocity. In this case, a two-way coupling between particles and fluid is needed to accurately represent the presence of particles on the fluid. Furthermore, due to differences in agglomerate morphology, it is not trivial to model the particle-fluid interaction without resolving the flow fluid around each particle. Attempts to correlate particle drag with particle volume fraction and Reynolds number include Ergun and Orning [18] who experimentally correlated pressure gradients in fluidized beds to the particle void fraction. Later studies by Hill et al. [19, 20] rely on the Lattice-Boltzmann Method (LBM) to resolve the flow around particles and correlate the drag force exerted on particles with particle volume fraction and the Reynolds number. While this method is highly accurate for homogeneous packing, the spatial variations in agglomerates that range from compact to dendritic in structure complicate the formulation of a general drag model. Dietzel and Sommerfeld [21] resolved the flow in agglomerates by local grid-refined Lattice-Boltzmann Method (LBM) simulations and correlated the overall drag force on different agglomerate morphologies to the projected cross section of the convex hull perpendicular to the mean flow direction. However, as the agglomerating and break-up mechanisms are governed by the particles being affected by different fluid forces, this approach is not suitable for this study.

While numerous studies on two-way coupled particle-fluid interactions have been reported, only a few account for the adhesive behaviour by fully resolving collision using the soft-sphere DEM approach. Afkhami et al. [22] studied the effect of particle adhesiveness using three different particle surface energy densities and showed a direct link between surface energy density and agglomeration rate.

The purpose of this study is look into how particle response time and particle adhesiveness affect the agglomeration rate. To obtain a fully-developed flow, the computational domain is made periodic in the streamwise direction. To avoid imposing any limitations on the agglomeration process, the soft-sphere DEM approach is used to resolve how particles collide, agglomerate, deposit and are re-entrained into the fluid due to collisions with other particles or by fluid forces. One advantage of the soft-sphere DEM approach is the fact that no additional models are required to account for agglomeration, agglomeration break-up, deposition and re-entrainment as all these processes are based directly on the particle properties and therefore automatically accounted for. Figure 1 gives an overview of these different processes.

2. Details on the numerical setup

2.1. Governing equations for fluid flow

The filtered LES equations governing unsteady, incompressible, three-dimensional viscous fluid flow in a periodic domain with two-way coupling between particle and fluid phases are the continuity and momentum equations

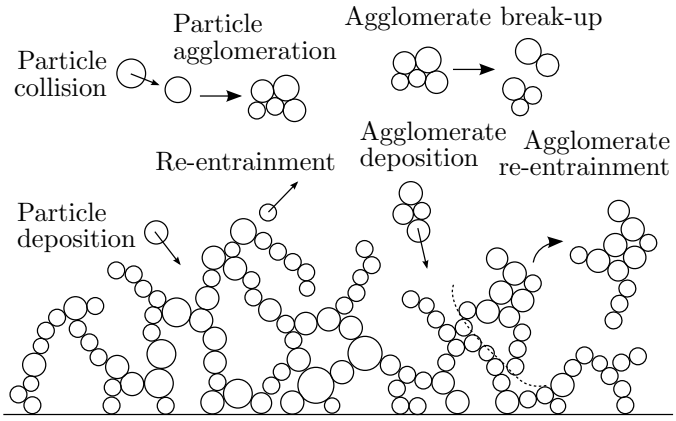

Figure 1: Overview of the different processes in the vicinity of a surface and away from a surface that are resolved directly by the soft-sphere DEM approach. The early stages of interest in this study are typically limited to particles colliding, particles agglomerating, agglomerates breaking up and single particles depositing at surfaces.

given by (1) and (2) respectively:

$$\frac{\partial\left(\alpha_{\mathrm{f}}\bar{u}_{\mathrm{i}}\right)}{\partial x_{\mathrm{i}}} = 0 \tag{1}$$

$$\frac{\partial\left(\alpha_{\mathrm{f}}\bar{u}_{\mathrm{i}}\right)}{\partial t} + \frac{\partial\left(\alpha_{\mathrm{f}}\bar{u}_{\mathrm{i}}\bar{u}_{\mathrm{j}}\right)}{\partial x_{\mathrm{j}}} = -\frac{\alpha_{\mathrm{f}}}{\rho_{\mathrm{f}}}\frac{\partial\bar{p}}{\partial x_{\mathrm{i}}} + \alpha_{\mathrm{f}}\frac{\partial}{\partial x_{\mathrm{j}}}\left(\left(\nu+\nu_{\mathrm{sgs}}\right)\frac{\partial\bar{u}_{\mathrm{i}}}{\partial x_{\mathrm{j}}}\right) - \frac{R_{\mathrm{pf}}}{\rho_{\mathrm{f}}} + \beta\delta_{1,\mathrm{i}} \tag{2}$$

where α_{f} is the local fluid volume fraction, $R_{\mathrm{pf}} = K_{\mathrm{pf}}(\boldsymbol{u} - \langle\boldsymbol{v}\rangle)$ is the momentum exchange with the particulate DEM phase and the $\beta\delta_{1,\mathrm{i}}$ term defines a momentum source term dynamically being changed to balance out the pressure gradient across the periodic domain. Different approaches exist to extrapolate the influence of particles onto the Eulerian grid. One approach is to extrapolate the influence of all particles to the nearest cell, which is shown in studies such as Garg et al. [23], Salman and Soteriou [24] to produce grid-dependent results. Instead, Capecelatro and Desjardins [25], Capecelatro et al. [26] suggest using a two-step filtering process. First, particle data is transferred to the Eulerian grid, which is afterwards diffused to ultimately give a filtering size Δx that is larger than the particle diameter, e.g. $\Delta x = 3d_{\mathrm{p}}$. In this work, the approach by Zhao and Shan [27] is adopted to represent the finite size of the particles on the Eulerian grid. Using this approach, the particle volume is divided into a finite number of non-overlapping elements of equal volume. The volume of each element is assumed to be located at the element centroid so that a particle may be present in more adjacent cells. This is especially import to obtain a correct representation of local particle volume fraction when the particle size approach the local grid size. Momentum is transferred from the particulate phase to the fluid phase using the implicit second-order accurate Crank-Nicolson scheme by summing up the fluid forces on the individual particles in each computational cell with volume V:

$$K_{\mathrm{pf}} = \frac{\alpha_{\mathrm{f}}\left|\sum_{\mathrm{i}}\boldsymbol{F}_{\mathrm{i,fluid}}\right|}{V\left|\boldsymbol{u} - \langle\boldsymbol{v}\rangle\right|} \tag{3}$$

The finite volume method is applied to discretise the governing equations. Time is advanced using an implicit second-order accurate scheme while all spatial terms are discretised using second-order accurate schemes. Pressure and velocity fields are coupled using the PISO algorithm [28].

The sub-grid scale viscosity ν_{sgs} accounts for sub-grid scale turbulence and naturally approaches zero in the case of DNS. In this study, focus is on LES where the sub-grid scale viscosity is modelled through the the wall-adapting local eddy-viscosity (WALE) model by Nicoud and Ducros [29]:

$$\nu_{\mathrm{sgs}} = \left(C_{\mathrm{w}}V^{1/3}\right)^2 \frac{\left(\bar{s}^{\mathrm{d}}_{\mathrm{ij}}\bar{s}^{\mathrm{d}}_{\mathrm{ij}}\right)^{3/2}}{\left(\bar{s}^{\mathrm{d}}_{\mathrm{ij}}\bar{s}^{\mathrm{d}}_{\mathrm{ij}}\right)^{5/2} + \left(\bar{s}^{\mathrm{d}}_{\mathrm{ij}}\bar{s}^{\mathrm{d}}_{\mathrm{ij}}\right)^{5/4}}, \tag{4}$$

where:

$$s^{\mathrm{d}}_{\mathrm{ij}} = \frac{1}{2}\left(\bar{g}^2_{\mathrm{ij}} + \bar{g}^2_{\mathrm{ji}}\right) - \frac{1}{3}\delta_{\mathrm{ij}}\bar{g}^2_{\mathrm{kk}}, \quad \bar{s}_{\mathrm{ij}} = \frac{1}{2}\left(\frac{\partial\bar{u}_{\mathrm{i}}}{\partial x_{\mathrm{j}}} + \frac{\partial\bar{u}_{\mathrm{j}}}{\partial x_{\mathrm{i}}}\right), \tag{5}$$

$$g_{\mathrm{ij}} = \frac{\partial\bar{u}_{\mathrm{i}}}{\partial x_{\mathrm{j}}}, \quad g^2_{\mathrm{ij}} = g_{\mathrm{ik}}g_{\mathrm{kj}} \tag{6}$$

with constant $C_{\mathrm{w}} = 0.325$ and where V is the local cell volume. Compared to the Smagorinsky-type models, the WALE model is more suited for wall-bounded flows, as the local sub-grid scale eddy-viscosity automatically goes to zero at the wall. Therefore, no dynamic constant adjusting or damping functions are needed to correct for walls.

2.2. Governing equations for particles

To model collisions of particles, the soft-sphere discrete element method (DEM) first proposed by Cundall and Strack [30] is used to track the translational and angular velocity throughout the simulations. For the i'th particle with mass m_{i}, radius r_{i} and mass moment of inertia $I_{\mathrm{i}} = (2/5)m_{\mathrm{i}}r^2_{\mathrm{i}}$, the position $\boldsymbol{x}_{\mathrm{i}}$ and angular velocity $\boldsymbol{\omega}_{\mathrm{i}}$ are governed by:

$$m_{\mathrm{i}}\frac{\mathrm{d}^2\boldsymbol{x}_{\mathrm{i}}}{\mathrm{d}t^2} = \boldsymbol{F}_{\mathrm{i,con}} + \boldsymbol{F}_{\mathrm{i,fluid}} \tag{7}$$

$$I_{\mathrm{i}}\frac{\mathrm{d}\boldsymbol{\omega}_{\mathrm{i}}}{\mathrm{d}t} = \boldsymbol{M}_{\mathrm{i,con}} + \boldsymbol{M}_{\mathrm{i,roll}} + \boldsymbol{M}_{\mathrm{i,fluid}} \tag{8}$$

where the $\boldsymbol{F}_{\mathrm{con}}$ is a contact force upon collision and $\boldsymbol{F}_{\mathrm{fluid}}$ is the combined fluid force acting on the particle. In the angular momentum equation, $\boldsymbol{M}_{\mathrm{con}}$ is the contact torque by a tangential off-set between colliding particles, $\boldsymbol{M}_{\mathrm{roll}}$ is the adhesive rolling resistance torque and $\boldsymbol{M}_{\mathrm{fluid}}$ is the torque caused by interaction with the fluid phase. That is, using the soft-sphere DEM approach, all the sub-processes depicted in figure 1 are automatically accounted for by

the most basic force and torque balances in (7) and (8) respectively. As a result no additional models are required to account for agglomeration, break-up, deposition and re-entrainment. Time is advanced using a velocity Verlet method [31], which is a second-order explicit method. When calculating the fluid forces acting on particles, the fluid velocity is interpolated to the particle centroid position. When solving the translational motion by (7), the particles may collide giving rise to contact forces. Checking for contact between all particles is a computational expensive task as the number of evaluations scales with the number of particles n_p as $n_\mathrm{p}(n_\mathrm{p}-1)/2$. Therefore, a list of potential collision partners, which is being updated every $10\Delta t_\mathrm{DEM}$ throughout the simulation, is used for collision detection to reduce computational time.

2.3. Fluid forces on particles

The motion of the individual particles is tracked using a lagrangian approach where the motion of individual particles is obtained by integrating (7) and (8) in time. In this study, the dominant fluid forces on the particles are the drag force and the shear and rotational lift forces. Gravity effects are neglected and the Brownian motion force is negligible for the particle size in this study.

For dispersed particles unaffected by the presence of nearby particles analytical Stokes solution predicts a drag coefficient $C_\mathrm{D} = 24/\mathrm{Re}_\mathrm{p}$. Different approaches exist to account for particle agglomeration. Using the approach by Breuer and Almohammed [32] and Sommerfeld and Stübing [12], each agglomerate is treated as an individual entity with an appropriate characteristic size, which is calculated based on the positions of the primary particles contained in the agglomerate. Using this approach, Dietzel and Sommerfeld [21] suggests using projected cross section of the convex hull wrapped around the agglomerate perpendicular to the flow direction to make the drag almost independent of agglomerate structure. However, treating agglomerates as individuals has some limitations for less adhesive particles where fluid shear cause agglomerates to break up. In fact, agglomerates may continuously deform and agglomerates may rupture into a number of smaller agglomerates [33], which is not straightforward to account for when treating agglomerates as individual entities [17]. In this study, we therefore track all primary particles by solving (7) and (8), which allows particles to continuously translate and roll over one another within an agglomerate. To account for clustering effects, we use the same approach as Marshall [13], Dizaji and Marshall [17], Marshall [34] to modify the Stokes drag as $C_\mathrm{D} = (24/\mathrm{Re}_\mathrm{p})F$, where $F = f(\mathrm{Re}_\mathrm{p}, \alpha_\mathrm{f})$. To account for particle clustering, Hill et al. [19, 20] did numerous flow-resolving Lattice-Boltzmann simulations of clustered particles and proposed a correlation to accurately predict drag at various volume fractions and particle Reynolds number. In the present study, we use the formulation by Benyahia et al. [35], which is based on the simulations by Hill et al. [19, 20], to account for a wider range of particle volume fractions and particle Reynolds numbers. In the limit of particles unaffected by the presence of other particles and low particle Reynolds number, F naturally approaches 1 so that Stokes drag is recovered. Due to complexity of these correlations, the reader is referred to Benyahia et al. [35] for the exact model formulation.

In this study, particles are affected by shear and rotational lift forces. By expressing the lift force in terms of a lift coefficient as $F_\mathrm{L} = C_\mathrm{L}(1/8)d_\mathrm{p}^2\rho_\mathrm{f}|\boldsymbol{u}-\boldsymbol{v}|^2$, the common Saffman solution [36] for lift due to shear can be recovered using the lift coefficient in (9) with $J^* = 1$ [37]:

$$C_\mathrm{L} = J^*\frac{12.92}{\pi}\sqrt{\frac{\omega^*}{\mathrm{Re}_\mathrm{p}}} \tag{9}$$

where $\omega^* = |\boldsymbol{\omega}|d_\mathrm{p}/|\boldsymbol{u}-\boldsymbol{v}|$ is the normalised undisturbed fluid vorticity at the particle centre. Correlations for $J^* = f(\epsilon)$, with $\epsilon = \sqrt{\omega^*/\mathrm{Re}_\mathrm{p}}$, are proposed by McLaughlin [38] in the limit of $\epsilon < 0.1$ or $\epsilon > 20$, while Mei [39] used tabulated values by McLaughlin [38] to propose a correlation for $0.1 \leq \epsilon \leq 20$. As shown by Bagchi and Balachandar [40], the combined lift of shear and rotation is the sum of a lift forces on a non-rotating particle in shear flow and a torque-free rotating particle in a uniform flow, which simply adds an term to (9). We use the experimental fit proposed by Loth and Dorgan [37], which is shown in predict experiments with reasonable accuracy up to $\mathrm{Re}_\mathrm{p} < 50$.

2.3.1. Contact forces

Due to the small size of the particles of interest, the van der Waals and electrostatic forces play dominant roles in the collision process, which ultimately results in particles agglomerating and depositing at walls. Based on properties and size of the particles, particle deformation in contact region upon collision may be important in the description of the adhesive force. In this study, the adhesive force is accounted for using the theory by Johnson-Kendall-Roberts (JKR) Johnson et al. [41], which is suitable for particles with $\lambda_\mathrm{T} = \left(4R\gamma^2/(E^2D_\mathrm{min}^3)\right)^{1/3} > 3$ [42], where γ is the surface energy density, defining half the energy required to separate two particles in contact and D_min is the minimum separation distance between two particles, which is commonly assumed to be 1.65 Å [43, 44].

Using the JKR model, the normal contact force upon collision is balanced by a spring force $\boldsymbol{F}_\mathrm{spring,n}$, an adhesive force $\boldsymbol{F}_\mathrm{jkr,n}$ and a damping force $\boldsymbol{F}_\mathrm{damp,n}$:

$$\boldsymbol{F}_\mathrm{spring,n} = -\frac{4E}{3R}a^3\boldsymbol{n} \tag{10}$$

$$\boldsymbol{F}_\mathrm{jkr,n} = 4\sqrt{\pi\gamma E a^3}\boldsymbol{n} \tag{11}$$

where the effective Young's modulus E and effective radius R are given by:

$$\frac{1}{E} = \frac{1-\nu_\mathrm{i}^2}{E_\mathrm{i}} + \frac{1-\nu_\mathrm{j}^2}{E_\mathrm{j}}, \qquad \frac{1}{R} = \frac{1}{r_\mathrm{i}} + \frac{1}{r_\mathrm{j}} \tag{12}$$

and the contact radius a is the radius of contact area. In equilibrium state where $\boldsymbol{F}_{\text{spring},} + \boldsymbol{F}_{\text{jkr,n}} = 0$, the contact radius is $a = (9\pi\gamma R^2/E)^{1/3} = a_0$. When using DEM, the overlap distance δ_n between particle i and j with positions $\boldsymbol{x}_\text{i}$ and $\boldsymbol{x}_\text{j}$ is calculated as $\delta_\text{n} = r_\text{i} + r_\text{j} - |\boldsymbol{x}_\text{i} - \boldsymbol{x}_\text{j}|$. For collisions following JKR theory, the relation between normal overlap δ_n and contact radius a is given by [44, 45]:

$$a^4 - 2R\delta_\text{n}a^2 - \frac{4\pi\gamma}{E}R^2a + R^2\delta_\text{n}^2 = 0 \tag{13}$$

which in this study is solved using the analytical solution derived by Parteli et al. [44]. Furthermore, the collision is damped by a normal damping force $\boldsymbol{F}_{\text{damp,n}}$ causing kinetic energy to be dissipated upon impact:

$$\boldsymbol{F}_{\text{damp,n}} = -2\sqrt{\frac{5}{6}}\beta\sqrt{S_\text{n}m}\boldsymbol{v}_\text{n} \tag{14}$$

with effective mass $m^{-1} = m_\text{i}^{-1} + m_\text{j}^{-1}$, $\boldsymbol{v}_\text{n}$ denoting the relative normal velocity, β accounting for the kinetic energy lost upon impact through the coefficient of restitution e and S_n taking the properties of the particles into account:

$$\beta = \frac{\ln(e)}{\sqrt{\ln^2(e) + \pi^2}} \tag{15}$$

$$S_\text{n} = 2E\sqrt{R\delta_\text{n}} \tag{16}$$

where e is material property. Due relatively low collision velocities, plastic deformation of particle material is not expected to be important. In the tangential direction, the spring force is given by:

$$\boldsymbol{F}_{\text{spring,t}} = -S_\text{t}\Delta s_\text{t} \tag{17}$$

where Δs_t is the tangential overlap and S_t takes particle properties into account through $S_\text{t} = 8G\sqrt{R\delta_\text{n}}$ with effective shear modulus G:

$$\frac{1}{G} = \frac{2-\nu_\text{i}}{G_\text{i}} + \frac{2-\nu_\text{j}}{G_\text{j}} \tag{18}$$

Like in the normal direction, energy is dissipated in the tangential direction, described by a tangential damping force:

$$\boldsymbol{F}_{\text{damp,t}} = -2\sqrt{\frac{5}{6}}\beta\sqrt{S_\text{t}m}\boldsymbol{v}_\text{t} \tag{19}$$

where $\boldsymbol{v}_\text{t}$ is the tangential relative velocity. As suggested by Thornton [46], Thornton and Yin [47], the total tangential force is in the case of JKR adhesion truncated to fulfil $|\boldsymbol{F}_{\text{con,t}}| \leq \mu_\text{s}|F_\text{N} + 2F_\text{C}|$ with μ_s and F_C being the sliding friction coefficient and the critical force required to separated agglomerated particles respectively.

2.3.2. Contact torques

In the case of adhesive particles, the formation of agglomerates and motion of particles on a surface tend to be dominated by particles rolling while particles sliding and twisting play negligible roles due to the small particle inertia [48, 49]. As a consequence of the deformed contact region described through JKR theory, the rolling motion differs from that of non-adhesive particles.

In the case of adhesive forces in the contact region between two particles or a particle and a wall, the point of contact stays behind the centre of mass projected onto the surface, which results in a torque opposing motion. This rolling resistance torque acts to obtain the equilibrium condition where the projected centre of mass and centre of contact are coincident. The rolling resistance torque is commonly described as proportional to the rolling displacement ξ, which is found by integrating the rolling velocity $\boldsymbol{v}_\text{r}$:

$$\xi = \left(\int_{t_0}^{t_1} \boldsymbol{v}_\text{r}(t)\text{d}t\right) \cdot \boldsymbol{t}_\text{r} \tag{20}$$

where $\boldsymbol{t}_\text{r} = \boldsymbol{v}_\text{r}/|\boldsymbol{v}_\text{r}$ is the direction of rolling. Based on the instantaneous rolling displacement ξ, the rolling resistance torque opposing motion is given by [50, 51]:

$$M_\text{r} = \begin{cases} k_\text{r}\xi & \text{if } \xi < \xi_\text{crit} \\ k_\text{r}\xi_\text{crit} & \text{if } \xi \geq \xi_\text{crit} \end{cases} \tag{21}$$

where the rolling stiffness is given by $k_\text{r} = 4F_\text{C}(a/a_0)^{3/2}$. When the particle is rolled a distance longer than a critical rolling displacement ξ_crit, the particle material slips and a new equilibrium contact region is found. The studies by Dominik and Tielens [50, 51] suggests that after rolling displacement reaches a critical value ξ_crit, the rolling resistance torque is constant. Based on experiments, Krijt et al. [52] suggests this critical rolling displacement to be linked to the equilibrium contact radius a_0 and a material dependent adhesion hysteresis parameter $\Delta\gamma/\gamma$ through:

$$\xi_\text{crit} = \frac{a_0}{12}\frac{\Delta\gamma}{\gamma} \tag{22}$$

A value $\Delta\gamma/\gamma = 0.5$ representing a typical value [52] is used throughout this study.

2.4. Non-dimensional groups

The results are reported based on a set of non-dimensional groups that govern different aspects of particle transport, particle collision and subsequently the agglomeration and deposition processes.

The numbers governing the transport of particles are the Reynolds number $\text{Re} = U \cdot D/\nu$, the dimensionless particle size $\epsilon = d_\text{p}/D$, the particle to fluid density ratio $\chi = \rho_\text{p}/\rho_\text{f}$, the integral time scale Stokes number $\text{St}_mathcalL = \tau_\text{p}/\tau_\mathcal{L}$ (or $\text{St}_\text{e} = \rho_\text{p}d_\text{p}^2U/(18\mu D) = \chi\epsilon^2\text{Re}/18$ in terms of eddy turn over time $\tau_\text{e} = D/U$) and the particle volume fraction defining the volume occupied by particles in the fluid domain $\phi = \sum_{n=1}^{N} V_\text{p}/(\sum_{n=1}^{N} V_\text{p} + V_\text{f})$.

Likewise, the collision and agglomeration processes are governed by a set of non-dimensional groups. The stiffness of a common collision is described by making the effective Young's modulus dimensionless using the particle density, bulk velocity and particle density forming $\lambda = E/(\rho_\mathrm{p} U^2)$. Likewise, to describe the sticking behaviour upon impact, the surface energy density, describing the strength of the adhesive force, is made non-dimensional by the particle density, bulk velocity and particle diameter, forming $\mathrm{Ad} = \gamma/(\rho_\mathrm{p} U^2 d_\mathrm{p})$.

Due to stiffness of most common materials, the time step size required to resolve particle collisions is typically in the order of nano seconds. A common approach to deal with the low time step sizes is to reduce the particle stiffness several orders of magnitude making collisions take place over longer time periods. For non-adhesive particles colliding without any plastic deformation, the rebound velocity is solely a function of velocity before collision and the coefficient of restitution. However, for collisions involving adhesive particles, the reduced particle stiffness has to be balanced by a reduction in adhesive intermolecular force so that the collision outcome remains the same. In this study, the high particle stiffness is reduced by decreasing the effective Young's modulus while modifying the surface energy density as:

$$\gamma_\mathrm{mod} = \gamma \left(\frac{E_\mathrm{mod}}{E} \right)^{2/5} \tag{23}$$

or in terms of the dimensionless elasticity parameter λ and adhesiveness parameter Ad:

$$\mathrm{Ad}_\mathrm{mod} = \mathrm{Ad} \left(\frac{\lambda_\mathrm{mod}}{\lambda} \right)^{2/5} \tag{24}$$

which is shown by Hærvig et al. [16] to make the collision outcome independent of a reduction in Young's modulus. For particles colliding in a viscous fluid, the fluid being forced away in the contact prior to collision may have a non-negligible effect on the rebound velocity. This importance of this effect is described through the collision Stokes number $\mathrm{St}^* = (m_\mathrm{p} + C_\mathrm{M} m_\mathrm{f})\, v/(6\pi\mu r_\mathrm{p})$, where $C_\mathrm{M} = 0.5$ is the added mass coefficient for spheres and v denotes the velocity before being affected by the surface. For solid particles colliding with $\mathrm{St}^* < 10$, Gondret et al. [53, 54], Legendre et al. [55] suggest all energy to be dissipated while this effect become almost negligible for $\mathrm{St}^* > 10^3$.

3. Results and validation

3.1. Fluid domain and discretisation

To make the results independent of stream-wise boundaries, the fluid domain is made periodic with a length longer than the elongated coherent turbulence structures in the boundary layer extending around $L_\mathrm{x}^+ \approx 1000$ [56]. In this study, a domain length of $L/D = 4$, corresponding to $L_\mathrm{x}^+ \approx 2500$ in viscous units, is chosen to make sure no coherent structures extend throughout the domain. Thus, the turbulence statistics are not affected by the size of the computational domain. A quarter of the cross-sectional mesh topology is shown in figure 2. As the agglomeration formation process takes place over stream-wise distances significantly longer than $L/D = 4$, the DEM domain is made periodic as well. In that way, the overall particle volume fraction ϕ stays constant throughout the simulation. This approach gives detailed information on the mechanisms governing agglomeration and deposition and how changes in fluid/particle properties affect early stages of agglomeration and deposition. Later stages of the deposition process where bridges and layers of multiple particles form, see figure 1, would require particles to be added throughout the simulation or a significantly higher initial particle concentration, which would alter the early stages of agglomeration and deposition processes.

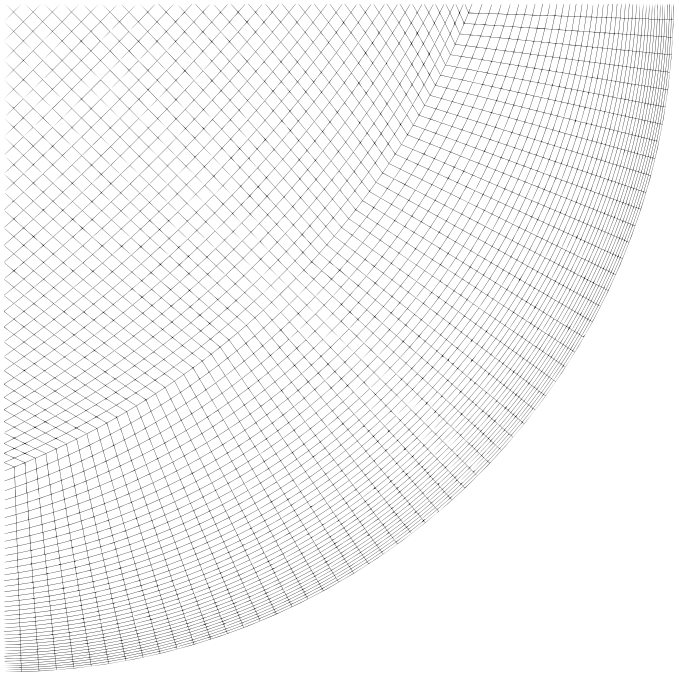

Figure 2: Mesh topology visualised by a quarter of the cross-sectional plane.

Table 1: Details of the three different meshes with θ, r and x denoting circumferential, radial and axial directions respectively. The mesh topology is shown in figure 2.

Resolution	$(N_\theta, N_\mathrm{r}, N_\mathrm{x})$	$\Delta\theta^+_\mathrm{max}$	Δx^+_max
Coarse	(160,90,160)	12	15
Medium	(200,110,200)	10	12.5
Fine	(240,140,240)	8	10

3.2. Validation of flow field

To validate the statistics of the flow field without particles added, the boundary layer velocity profile is compared for the different meshes listed in table 1. The

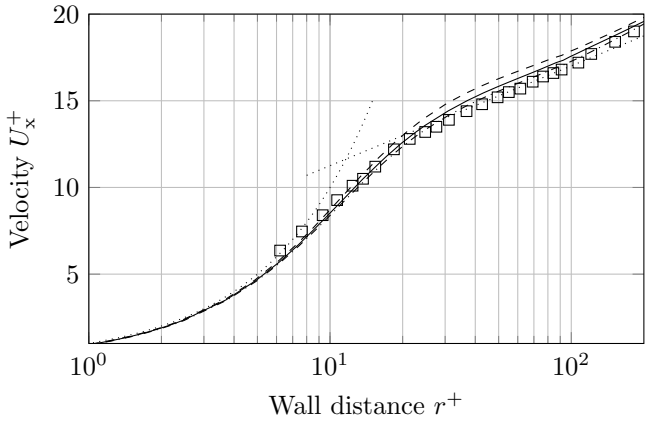

Figure 3: Time-averaged turbulent boundary layer velocity profile for $\mathrm{Re} = UD/\nu = 10,000$ for different mesh resolutions, see table 1: (- - -) Coarse resolution LES; (——) Medium resolution LES; (-·-·-) Fine resolution LES; (·····) Viscous sub-layer with $U_x^+ = r^+$ and log-law layer with $U_x^+ = 2.5\ \ln(r^+) + 5.5$; □ Experiment for $\mathrm{Re} = 10,000$ by den Toonder and Nieuwstadt [57].

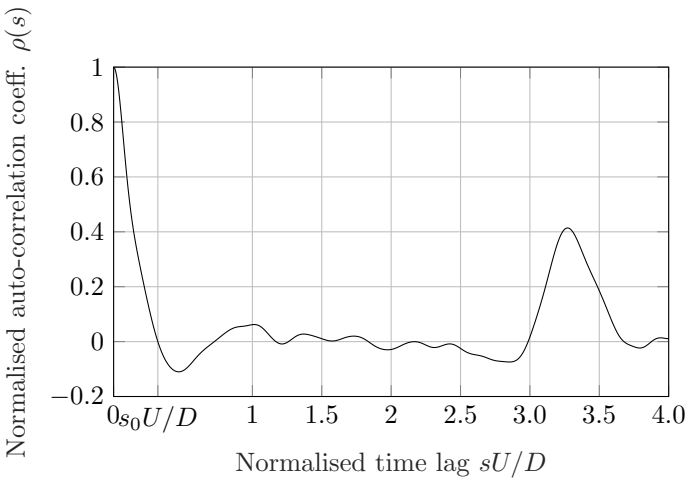

Figure 4: Auto-correlation of the stream-wise velocity signal sampled at the centre-line of the pipe $\rho(s) = \langle u_x(t)u_x(t+s)\rangle \,/\, \langle u_x(t)^2\rangle$.

various grid resolutions are compared to both experiments by den Toonder and Nieuwstadt [57] and boundary layer theory. The time-averaged flow field is found by averaging over a time period of $t^+ = t \cdot U/D = 400$ after which the mean flow field statistics are found to be independent of time. Figure 3 shows how the numerical simulations compare to boundary layer theory and experiments at $\mathrm{Re} = 10,000$. As seen in figure 3, the more resolving LES simulations approach the experiment by den Toonder and Nieuwstadt [57].

3.3. Simulation Parameters

Particles with diameter $\epsilon = d_p/D = 5 \cdot 10^{-3}$ are transported in a turbulent pipe flow with $\mathrm{Re} = U \cdot D/\nu = 10,000$.Variations in particles response time are introduced by changes in particle density. The particle response time is commonly made non-dimensional by either integral time scale of the turbulence $\tau_\mathcal{L}$, which gives a measure of the largest eddies being resolved, the Kolmogorov time scale τ_η or the large eddy turn over time $\tau_e = D/U$. In this study, the results are reported based on the integral time scale of the flow and eddy turn over time forming $\mathrm{St}_\mathcal{L} = \tau_p/\tau_\mathcal{L}$ and $\mathrm{St}_e = \tau_p/\tau_e$ respectively. The integral time scale of the turbulence is found by [58]:

$$\tau_\mathcal{L} = \int_0^{s_0} \rho(s)\mathrm{d}s \tag{25}$$

where the normalised auto-correlation coefficient $\rho(s) = \langle u_x(t)u_x(t+s)\rangle \,/\, \langle u_x(t)^2\rangle$ is found for the stream-wise velocity signal at the centre-line of the pipe, see figure 4. Instead of integrating to infinity in equation (25), we choose to integrate to s_0 to avoid any slight periodicity of the turbulent field extending throughout the periodic domain with a finite length $L = 4D$ that may artificially overestimate the integral time scale [59], such as observed by the peak at $sU/D \approx 3.3$ in figure 4. The Stokes number based on the large eddy turn over time $\mathrm{St}_e = \tau_p/\tau_e = \rho_p d_p^2 U/(18\mu D)$ can be re-written in terms of Re, ϵ and density ratio $\chi = \rho_p/\rho_f$ as $\mathrm{St}_e = \chi\epsilon^2\mathrm{Re}/18$. The particles are affected by an inter-particle adhesive force characterised by a surface energy density γ and develop a slightly flattened contact region upon collision as predicted by JKR theory. The particle adhesiveness is characterised by the adhesiveness parameter $\mathrm{Ad} = \gamma/(\rho_p U^2 d_p)$, which in the limit of $\mathrm{Ad} = 0$ corresponds to non-adhesive particles. For particles in contact, the adhesive force is balanced by the repulsive Hertzian force characterised by the effective Young's modulus E, which describes the particle stiffness. The particle stiffness is non-dimensional using the elasticity parameter $\lambda = E/(\rho_p U^2)$ and the damping upon collision by the coefficient of restitution e, which describes the ratio of relative velocity after and before impact in case of non-adhesive particles, e.g. $\mathrm{Ad} = 0$. When $\mathrm{Ad} > 0$, the adhesive force acts to dissipate energy upon collision so that $e_{\mathrm{eff}} < e$, which in the limit when particles stay adhered upon contact results in $e_{\mathrm{eff}} = 0$.

The particles are initially placed randomly throughout the turbulent flow so that no particles are in contact at $t^+ = 0$. Instead of using a more or less sophisticated approach to prescribe the initial velocity of particles, the particles are inserted with zero velocity in the present study. A constant particle volume fraction $\phi = 10^{-3}$ corresponding to $n_p \approx 50000$ is used in all simulations.

Using the soft-sphere DEM approach, the collision processes are resolved directly using (7). To resolve collisions that typically takes place over time intervals of microseconds, a time step size in the order of nano seconds is typically needed. As the turbulent flow modelled using LES can be resolved using a time step size, which is several orders of magnitude higher, the particles and fluid phases are advanced using two different time step sizes. The fluid time step size is determined so that the maximum

cell convective Courant number is 0.5, corresponding to a time scale ratio of the characteristic fluid time scale and fluid time step size $D/(U\Delta t_{\mathrm{CFD}}) = 160$. The particulate DEM phase is advanced using a time step size $\Delta t_{\mathrm{CFD}}/\Delta t_{\mathrm{DEM}} = 500$, which is shown by simple binary collisions to be sufficient to resolve collisions so that the collision outcome is unaffected by the time step size.

3.4. Overview of simulations

The following gives an overview of the different simulations carried out in the present study. The simulation parameters are summarised in terms of non-dimensional numbers in table 2.

Simulation no. 1–21. Depending on the Stokes number, the particles will be affected by different turbulence scales. As the Stokes number approaches zero, the particles will be affected by increasingly smaller eddies. In this study where LES is used, it is important that particles are unaffected by the eddies not being resolved. Therefore, simulations with varying Stokes number $\mathrm{St_e} = 0.4 \cdot 2^x$ ($\mathrm{St}_{\mathcal{L}} = 2.9 \cdot 2^x$), $x = 0\,..\,6$ and carried out using the three meshes listed in table 1.

Simulation no. 22–28. As already mentioned, the agglomeration processes considered in this study have elasticity parameter $\lambda \approx 500 \cdot 10^3$. Using this value, particle-particle and particle-wall collisions happen over time intervals in the order of nano seconds. To reduce computational time, a modified elasticity parameter is introduced: $\lambda_{\mathrm{mod}} = \lambda \cdot 0.001 = 500$. By reducing the elasticity parameter, the particles behave more adhesive. Therefore, to ensure the collision outcome stays independent of reduction in elasticity parameter, the criterion in (24) is used to reduce the adhesiveness parameter so that $\mathrm{Ad}_{\mathrm{mod}} = 0.08 \cdot 0.001^{2/5} = 0.005$. However, as noted in the study, introducing a lower adhesiveness parameter also reduces the critical force $F_{\mathrm{C}} = 3\pi R\gamma$ required to separate two agglomerated particles. Therefore, simulations 22–28 are carried out with $\lambda_{\mathrm{mod}} = \lambda/100$ instead of $\lambda_{\mathrm{mod}} = \lambda/1000$ to ensure the agglomeration rate is in fact independent of a reduction in elasticity and adhesiveness parameter.

Simulation no. 29–35. The purpose of simulation 29–35 is to investigate the transition from particles being almost non-adhesive to particles being highly adhesive. For this purpose, the adhesive parameter is varied in the range 0.001 to 0.064 at a constant Stokes number $\mathrm{St_e} = 1$ or in terms of integral time scale $\mathrm{St}_{\mathcal{L}} = 7.3$ (simulations 29–35)

Simulation no. 36–42. These simulations are carried out for non-adhesive particles (e.g. Ad = 0) over the full range of Stokes numbers considered in this study.

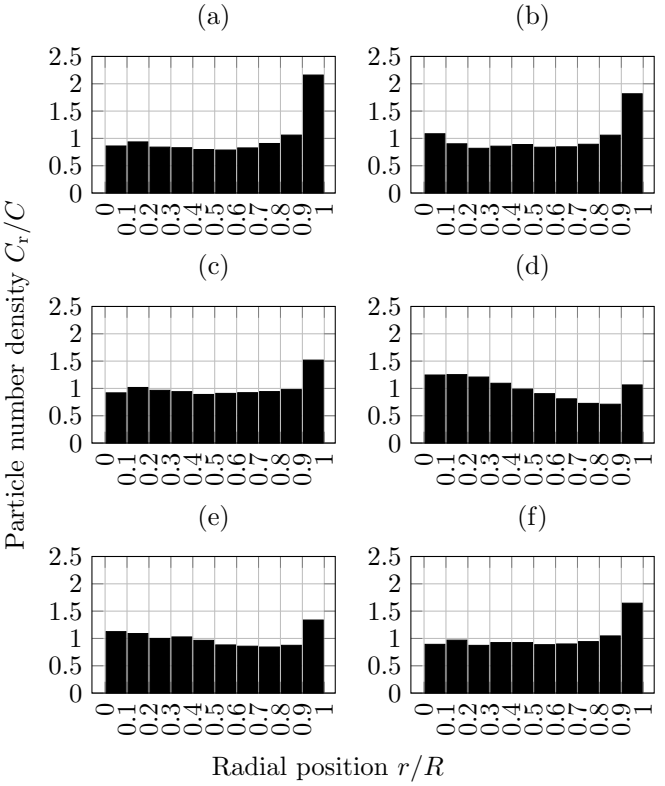

Figure 5: Particle number density in different radial sections of the pipe normalised by the average number density in the different radial section of the pipe C_{r}/C for non-adhesive particles with Ad = 0 at time $t^+ = tU/D = 100$, see simulation no. 36–42 in table 2 for simulation parameters: (a) $\mathrm{St_e} = 0.8$, $\mathrm{St}_{\mathcal{L}} = 5.8$; (b) $\mathrm{St_e} = 1.6$, $\mathrm{St}_{\mathcal{L}} = 11.6$; (c) $\mathrm{St_e} = 3.2$, $\mathrm{St}_{\mathcal{L}} = 23.2$; (d) $\mathrm{St_e} = 6.4$, $\mathrm{St}_{\mathcal{L}} = 46.4$; (e) $\mathrm{St_e} = 12.8$, $\mathrm{St}_{\mathcal{L}} = 92.8$; (f) $\mathrm{St_e} = 25.6$, $\mathrm{St}_{\mathcal{L}} = 185.6$.

3.5. Non-adhesive particles

Figure 5 shows how non-adhesive particles tend to gather in different radial sections of the pipe based on their response times. Figure 5 shows how changes in particle response time cause particles to accumulate in different radial section of the fully-developed turbulent pipe flow. For all particle response times, there is a peak in particle concentration in the outermost section of the pipe close to the wall at $0.9 < r/R < 1$. For either low or high particle response times, the particles attain a uniform concentration profile throughout the pipe. At an intermediate particle response time of $\mathrm{St_e} = 6.4$, the particle concentration increases towards the centre of the pipe. Figure 6(a) to 6(c) show how changes in Stokes number from $\mathrm{St_e} = 0.8$ to $\mathrm{St_e} = 6.4$ and $\mathrm{St_e} = 25.6$ affect preferential clustering of particles.

3.6. Effect of sub-grid scale turbulence eddies on particle agglomeration

As the smallest eddy scales are modelled by a sgs-model, it is important that these unresolved scales do not affect particle motion and subsequently agglomeration and deposition. Ultimately, as particles with sufficiently

Table 2: Details on the simulations in terms of non-dimensional groups: Flow Reynolds number $\mathrm{Re} = U \cdot D/\nu$, particle size $\epsilon = d_\mathrm{p}/D$, Eddy turn over time ($\tau_\mathrm{e} = D/U$) Stokes number $\mathrm{St_e} = \tau_\mathrm{p}/\tau_\mathrm{e} = \chi\epsilon^2\mathrm{Re}/18$, Integral time scale Stokes number $\mathrm{St}_\mathcal{L} = \tau_\mathrm{p}/\tau_\mathcal{L}$, elasticity parameter $\lambda = E/(\rho_\mathrm{p}U^2)$, adhesiveness parameter $\mathrm{Ad} = \gamma/(\rho_\mathrm{p}U^2 d_\mathrm{p})$, coefficient of restitution e, particle volume fraction ϕ and LES resolution (see table 1). The integer x is used to describe a range of simulation parameters.

No.	x	Re	ϵ	$\mathrm{St_e}$	$\mathrm{St}_\mathcal{L}$	λ	Ad	e	ϕ	LES res.
1–7	$0\,..\,6$	10^4	0.005	$0.4 \cdot 2^x$	$2.9 \cdot 2^x$	500	0.05	0.3	10^{-3}	Coarse
8–14	$0\,..\,6$	10^4	0.005	$0.4 \cdot 2^x$	$2.9 \cdot 2^x$	500	0.05	0.3	10^{-3}	Medium
15–21	$0\,..\,6$	10^4	0.005	$0.4 \cdot 2^x$	$2.9 \cdot 2^x$	500	0.05	0.3	10^{-3}	Fine
22–28	$0\,..\,6$	10^4	0.005	$0.4 \cdot 2^x$	$2.9 \cdot 2^x$	5000	$0.05 \cdot 10^{2/5}$	0.3	10^{-3}	Medium
29–35	$0\,..\,6$	10^4	0.005	1	7.3	500	$0.001 \cdot 2^x$	0.3	10^{-3}	Medium
36–42	$0\,..\,6$	10^4	0.005	$0.4 \cdot 2^x$	$2.9 \cdot 2^x$	500	0	0.3	10^{-3}	Medium

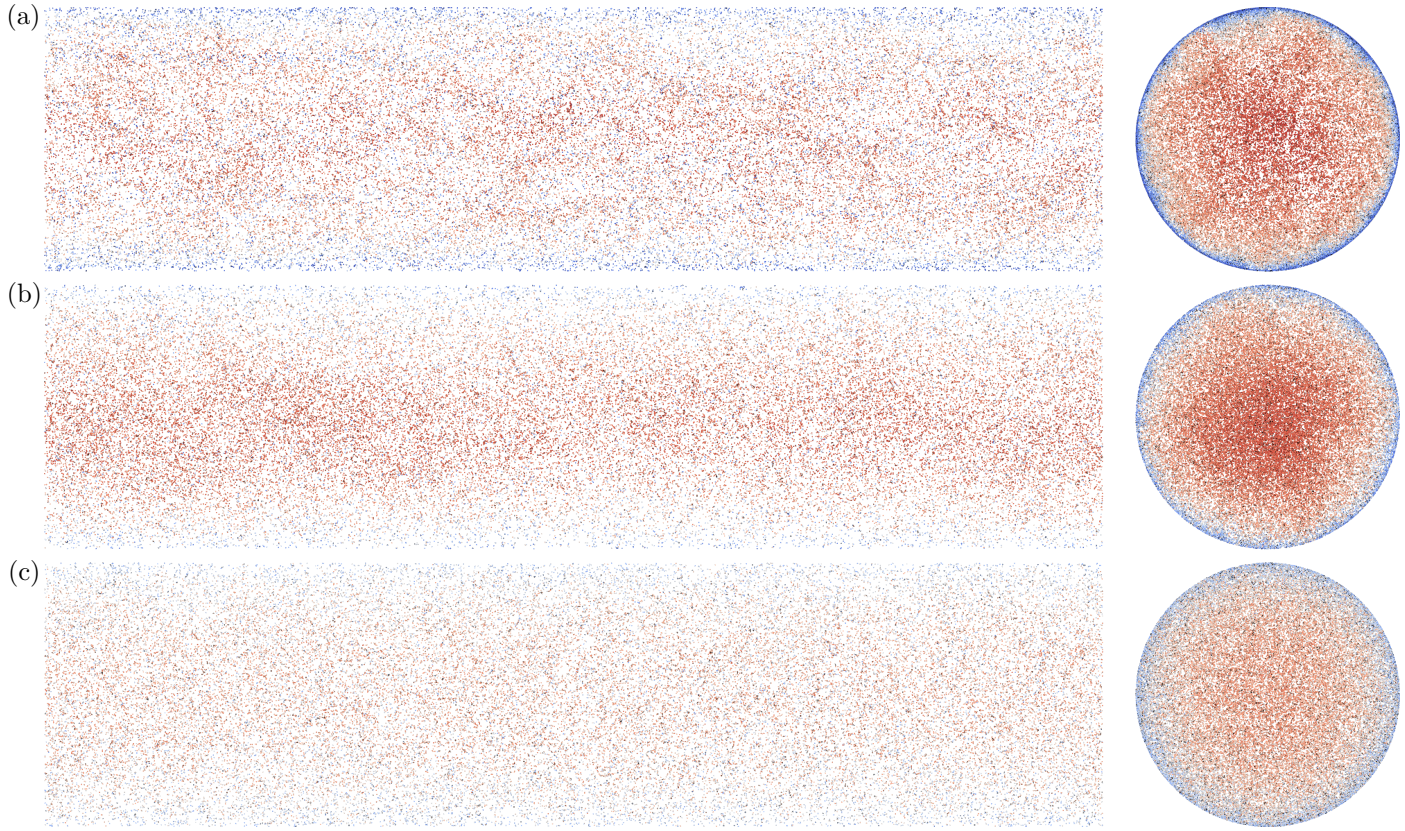

Figure 6: Overview of transport of non-adhesive particles (e.g. Ad = 0) at time $t^+ = tU/D = 100$: (a) $\mathrm{St_e} = 0.8$, $\mathrm{St}_\mathcal{L} = 5.8$; (b) $\mathrm{St_e} = 6.4$, $\mathrm{St}_\mathcal{L} = 46.4$; (c) $\mathrm{St_e} = 25.6$, $\mathrm{St}_\mathcal{L} = 185.6$. For simulation properties see simulation no. 23, 26 and 28 in table 2 respectively. The particles are coloured according to their instantaneous velocity magnitude. The reader is referred to the online version of this article for a better interpretation.

low response time, e.g. tracer particles, would respond to all turbulence scales, a DNS solution would be required in this case. However, as pointed out by Armenio et al. [60], particles with finite mass do not respond to smaller turbulence scales, suggesting LES to be an appreciate method to investigate particles interactions in a turbulent flow. Figure 7 shows how changes in mesh resolution affect the average number of particles per agglomerate. Due to finite response times of the particles considered, the grid independence analysis is carried out for a wide of particle Stokes numbers. As the figure shows, results obtained for particles with $\mathrm{St_e} = \mathcal{O}(10)$ are only slightly affected by changes in mesh resolution. This suggests these particles to be less affected by the smaller eddies not being resolved by the coarsest mesh. For the most responsive particles with $\mathrm{St_e} = 0.4$, there is a slightly more pronounced difference between the coarse and the finer meshes, suggesting the particles with $\mathrm{St_e} = 0.4$ to respond to the eddies not being resolved by the coarsest mesh. Due to the minor differences between the medium and fine resolution meshes, the medium resolution mesh from table 1 is used throughout this study.

3.7. Effect of introducing softer particles

In the present study, the particle elasticity parameter is reduced by a factor 1000 from a realistic value of $\lambda = 500 \cdot 10^3$ to $\lambda_\mathrm{mod} = 500$ to decrease computational time. As the stiffness is reduced, the particles overlap

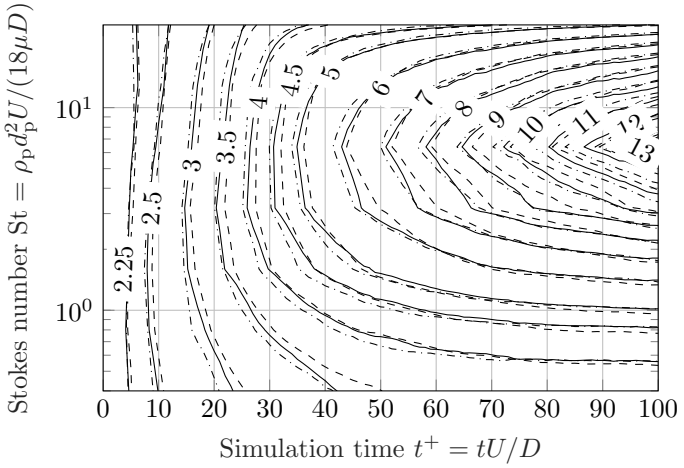

Figure 7: Effect of changes in mesh resolution, see table 1, and Stokes number on particle agglomeration visualised by the average number of particles per agglomerate. See simulation no. 1–21 in table 2 for simulation parameters: (- - -) Coarse resolution LES; (——) Medium resolution LES; (-·-·-) Fine resolution LES.

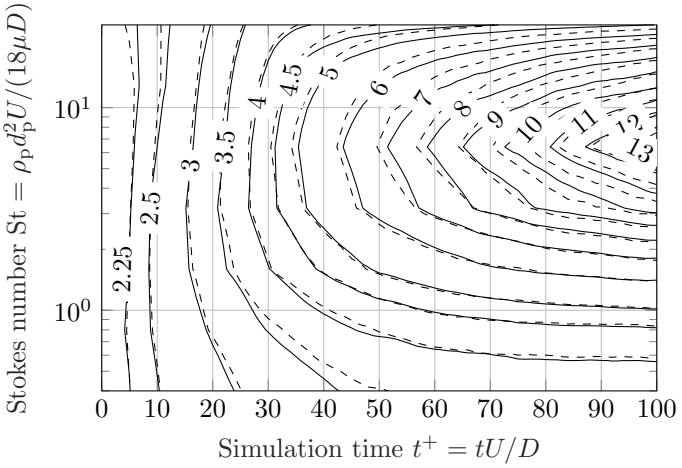

Figure 8: Effect of introducing softer particles with a reduced elasticity parameter when using the criterion in (24). Contours show particle agglomeration rate visualised by the average number of particles per agglomerate for particle elasticity parameters $\lambda = 500$ and $\lambda = 5000$. See simulation no. 8–14 and 22–28 in table 2 for simulation parameters: (——) $\lambda_1 = 500$, $\mathrm{Ad}_1 = 0.05$; (- - -) $\lambda_2 = 5000$, $\mathrm{Ad}_2 = \mathrm{Ad}_1 \cdot (\lambda_2/\lambda_1)^{2/5}$.

slightly more upon impact, which allows for an increased particle time step size. In order for the collision outcome (sticking/rebounding) to remain the same despite a reduced particle stiffness, the particle adhesiveness is modified using the criterion given in (24). Using this criterion, the modified collision duration $t_{\mathrm{col,mod}}$ scales as $\Delta t_{\mathrm{col,mod}} = \Delta t_{\mathrm{col}} \left(\lambda/\lambda_{\mathrm{mod}}\right)^{2/5}$ [16]. To ensure that the agglomeration process is in fact independent of the change in elasticity parameter, an additional set of simulations with $\lambda = 5000$ is carried out and compared to $\lambda = 500$. Figure 8 shows average number of particles per agglomerate as function of time and at various Stokes numbers for $\lambda_1 = 500$ and $\lambda_2 = 5000$ with adhesiveness parameters $\mathrm{Ad}_1 = 0.05$ and $\mathrm{Ad}_2 = \mathrm{Ad}_1(\lambda_2/\lambda_1)^{2/5}$. As figure 8 shows, the agglomeration process is in fact almost independent of a change in elasticity parameter from $\lambda = 500$ to $\lambda = 5000$ when reducing the adhesiveness parameter by (24) for particles with Stokes numbers in the range $\mathrm{St_e} = 0.4$ to $\mathrm{St_e} = 25.6$.

3.8. Effect of particle Stokes number on agglomeration and deposition

As already shown in figure 7, the Stokes number significantly affects the agglomeration behaviour in terms of average number of particles per agglomerate, which can be directly linked to a change in collision mechanism. The most responsive particles with $\mathrm{St_e} \ll 1$ approach tracer particles and closely follow fluid stream lines. As a result, particles collide due to their finite size while following neighbouring stream lines. The less response particles with $\mathrm{St_e} < 1$ are only slightly affected by the fluctuating flow and mainly follow the average flow. Figure 9(a) to 9(c) gives an visual overview of how changes in Stokes number from $\mathrm{St_e} = 0.8$ to $\mathrm{St_e} = 6.4$ and $\mathrm{St_e} = 25.6$ affect the agglomeration and deposition processes. As figure 9 shows, the agglomeration process is highly affected by the Stokes number with the largest agglomerates being formed at moderate Stokes numbers, see figure 9(b). This is in agreement with the results in figure 7 showing that at either lower or higher Stokes numbers the average number of particles per agglomerate decreases significantly. Figure 10 shows the fraction of particles contained in agglomerates at various Stokes numbers. As the figure shows, the fraction of particles contained in agglomerates at $t^+ = 100$ is almost independent of a change in Stokes numbers for lower Stokes numbers. For higher Stokes numbers, e.g. $\mathrm{St_e} > 6.4$ ($\mathrm{St}_{\mathcal{L}} > 46.4$), the fraction of particles contained in agglomerates is highly dependent on the Stokes number, where higher Stokes numbers result in a lower fraction of agglomerated particles. This can be explained by a decrease in collision rate for higher Stokes numbers. Furthermore, studies such as Zhao et al. [61] suggest the slip velocity between fluid and particles and therefore only variations in drag force to generally increase with the Stokes numbers, which may explain why only smaller agglomerates are found for higher Stokes numbers as higher variations in drag force may cause agglomerates to break up again.

Furthermore, as depicted visually in figure 9, the radial agglomerate number density varies with the Stokes number. Figures 11(a) to 11(d) show spatial variations of agglomerate number density in different radial sections of the pipe C_{r} normalised by the average agglomerate number density for the radial sections C for a low Stokes number $\mathrm{St_e} = 0.8$ at times $t^+ = 25$, $t^+ = 50$, $t^+ = 75$ and $t^+ = 100$. For all times the agglomerate number density is highest in the outer section near the wall, where particles stick to the wall and agglomerate. As seen in

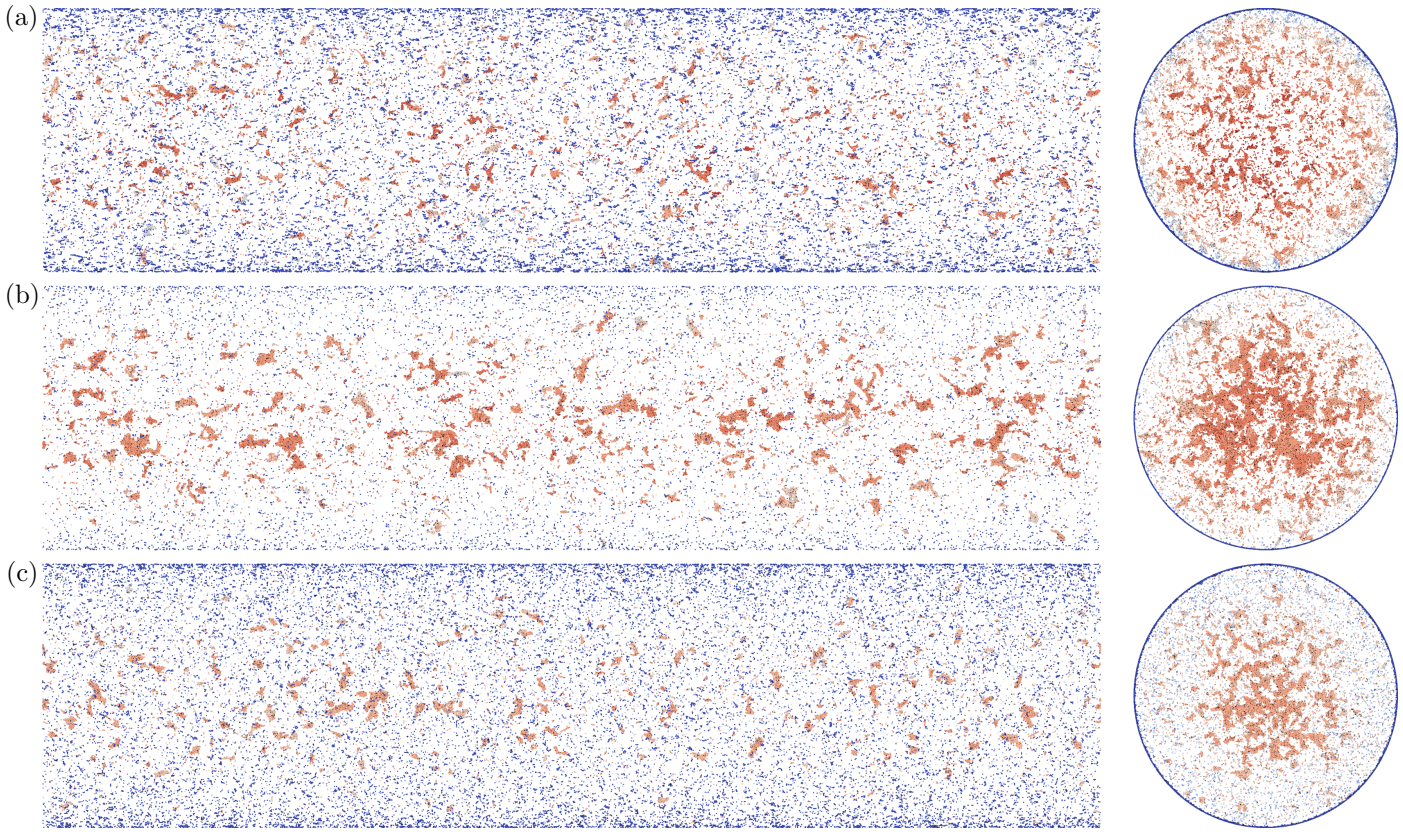

Figure 9: Agglomerating and depositing behaviour at time $t^+ = tU/D = 100$: (a) $\mathrm{St_e} = 0.8$, $\mathrm{St_{\mathcal{L}}} = 5.8$; (b) $\mathrm{St_e} = 6.4$, $\mathrm{St_{\mathcal{L}}} = 46.4$; (c) $\mathrm{St_e} = 25.6$, $\mathrm{St_{\mathcal{L}}} = 185.6$. For simulation properties see simulation no. 9, 12 and 14 in table 2 respectively. The particles are coloured according to their instantaneous velocity magnitude. The reader is referred to the online version of this article for a better interpretation.

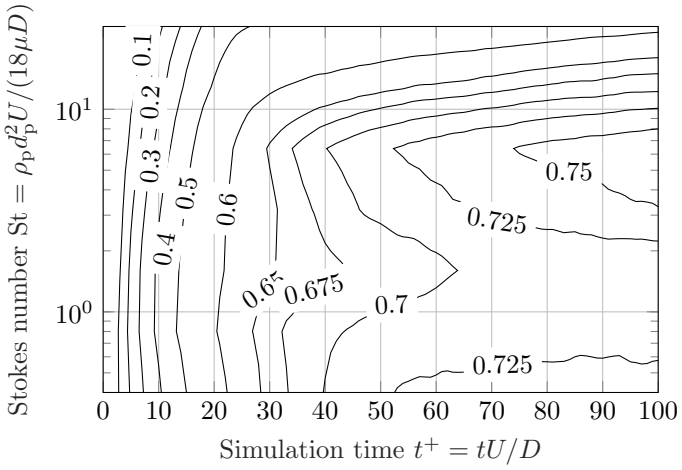

Figure 10: Fraction of particles contained in agglomerates at various Stokes numbers as function of simulation time. See simulation no. 8–14 in table 2 for simulation parameters.

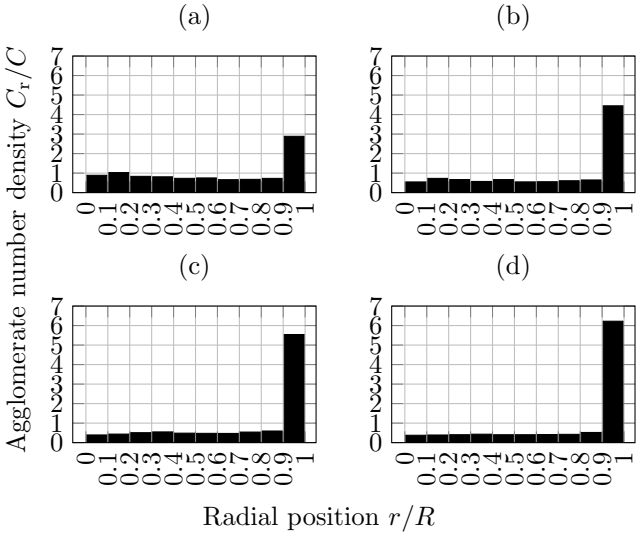

Figure 11: Agglomerate number density in different radial sections of the pipe normalised by the average agglomerate number density in the different radial section of the pipe C_r/C at Stokes number $\mathrm{St_e} = 0.8$ ($\mathrm{St_{\mathcal{L}}} = 5.8$), see simulation no. 9 in table 2 for simulation parameters: (a) $t^+ = tU/D = 25$; (b) $t^+ = tU/D = 50$; (c) $t^+ = tU/D = 75$; (d) $t^+ = tU/D = 100$.

figure 11(a) for $t^+ = 25$, there is a slight increase in agglomerate number density towards the centre of the pipe. At times $t^+ = 50$, $t^+ = 75$ and $t^+ = 100$, the agglomerate number density profile is almost constant away from the wall, while the number of agglomerates near the wall continues to increase. Figure 12 show spatial agglomerate number densities for particles with $\mathrm{St} = 6.4$ ($\mathrm{St_{\mathcal{L}}} > 46.4$). At a slightly higher Stokes number $\mathrm{St_e} =$

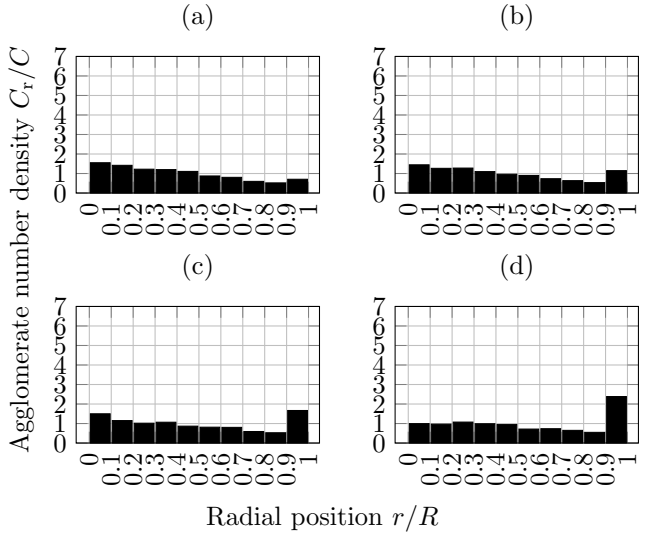

Figure 12: Agglomerate number density in different radial sections of the pipe normalised by the average agglomerate number density in the different radial section of the pipe C_r/C at Stokes number $\mathrm{St} = 6.4$ ($\mathrm{St}_\mathcal{L} > 46.4$), see simulation no. 12 in table 2 for simulation parameters: (a) $t^+ = tU/D = 25$; (b) $t^+ = tU/D = 50$; (c) $t^+ = tU/D = 75$; (d) $t^+ = tU/D = 100$.

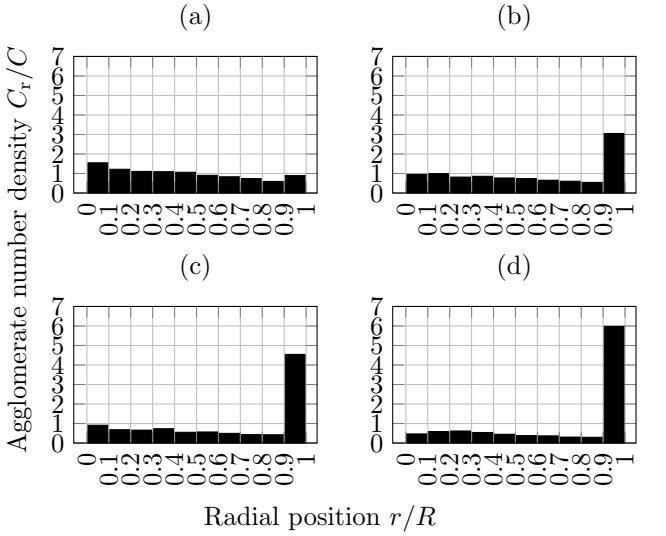

Figure 13: Agglomerate number density in different radial section of the pipe normalised by the average agglomerate number density in the different radial section of the pipe C_r/C at Stokes number $\mathrm{St_e} = 25.6$ ($\mathrm{St}_\mathcal{L} = 185.6$), see simulation no. 14 in table 2 for simulation parameters: (a) $t^+ = tU/D = 25$; (b) $t^+ = tU/D = 50$; (c) $t^+ = tU/D = 75$; (d) $t^+ = tU/D = 100$.

6.4 ($\mathrm{St}_\mathcal{L} = 46.4$), there is a more distinct agglomerate clustering in the centre of the pipe. As opposed to the agglomeration process for the more responsive particles in figure 11, significantly less agglomerates are found in the section near the wall. As already shown in figure 7 the average agglomerate size is highest for intermediate Stokes numbers $\mathrm{St_e} \approx 6.4$ ($\mathrm{St}_\mathcal{L} \approx 46.4$), which effectively traps particles in larger agglomerates. As agglomerates increase in size, the effective response time increase so that shear lift force effectively cause agglomerates to drift towards the centre of the pipe. Figure 13(a) to 13(d) show spatial agglomerate number densities for less response particles with $\mathrm{St_e} = 25.6$ ($\mathrm{St}_\mathcal{L} = 185.6$). As shown in figure 13(a) for $t^+ = 25$ the agglomerate number density is highest in the centre of the pipe suggesting the agglomerates to primarily start forming here. At $t^+ = 50$, $t^+ = 75$ and $t^+ = 100$ the highest agglomerate number densities are found near the wall, where particles stick to the surface.

3.9. Effect of particle adhesiveness on agglomeration

The particle adhesiveness is varied through the surface energy density γ, resulting in adhesiveness parameters in the range $\mathrm{Ad} = 0.001$ to $\mathrm{Ad} = 0.064$ (see simulation no. 22–28). This range covers particles that are unaffected by adhesive forces to highly adhesive particles. Figure 14(a) to 14(c) gives an visual overview of how changes in adhesiveness parameter from $\mathrm{Ad} = 0.016$ to $\mathrm{Ad} = 0.032$ and $\mathrm{Ad} = 0.064$ affect the agglomeration process for particles with $\mathrm{St} = 1$ ($\mathrm{St}_\mathcal{L} = 7.3$) after $t^+ = 100$. As shown in figure 14(a) the less adhesive particles with $\mathrm{Ad} = 0.016$ only form smaller agglomerates that are generally located towards the centre of the pipe. The more adhesive particles with $\mathrm{Ad} = 0.032$ and $\mathrm{Ad} = 0.064$ in figure 14(b) and 14(c) form larger agglomerates and the strength of the adhesive force is sufficient to deposit particles on the wall. Figure 15 shows how the fraction of particles contained in agglomerate varies with adhesiveness parameter for particles with $\mathrm{St_e} = 1$ ($\mathrm{St}_\mathcal{L} = 7.3$). As shown in figure 15, the variations in adhesiveness parameter greatly affect the fraction of particles being trapped in agglomerates. For all the cases, the agglomeration process attains a steady-state, where the agglomeration rate equals the break-up rate so that the fraction of particles agglomerated is independent of simulation time after $t^+ \approx 80$. After $t^+ \approx 80$ the fraction of particles contained in agglomerates range from below 0.03 to above 0.7 for the most adhesive particles. As the elastic collisions are fully-resolved over numerous time steps using the soft-sphere DEM approach in the present study, even non-adhesive particles (simulation no. 36–42) with $\mathrm{Ad} = 0$ resulting in a small but finite fraction of particles contained in agglomerated. For the non-adhesive particles, the fraction of particles agglomerated is below 0.003. Figure 16 shows how changes in adhesiveness parameter affects the average number of particles contained in agglomerates for particles with $\mathrm{St} = 1$ ($\mathrm{St}_\mathcal{L} = 7.3$). Figure 16 shows how the adhesiveness parameter greatly affects the size of the agglomerates being formed in the flow. For all cases the average number of particles contained in agglomerates remains constant in time after $t^+ \approx 90$. That is, the strength of the adhesive force is insufficient to keep the particles agglomerated so that the larger agglomerates break up into smaller agglomerates either due to collisions with other particles or due to shear in the flow field. Figure 17 shows how an increase in adhesiveness parameter from $\mathrm{Ad} = 0.002$ to $\mathrm{Ad} = 0.064$ affects the local agglomerate number density

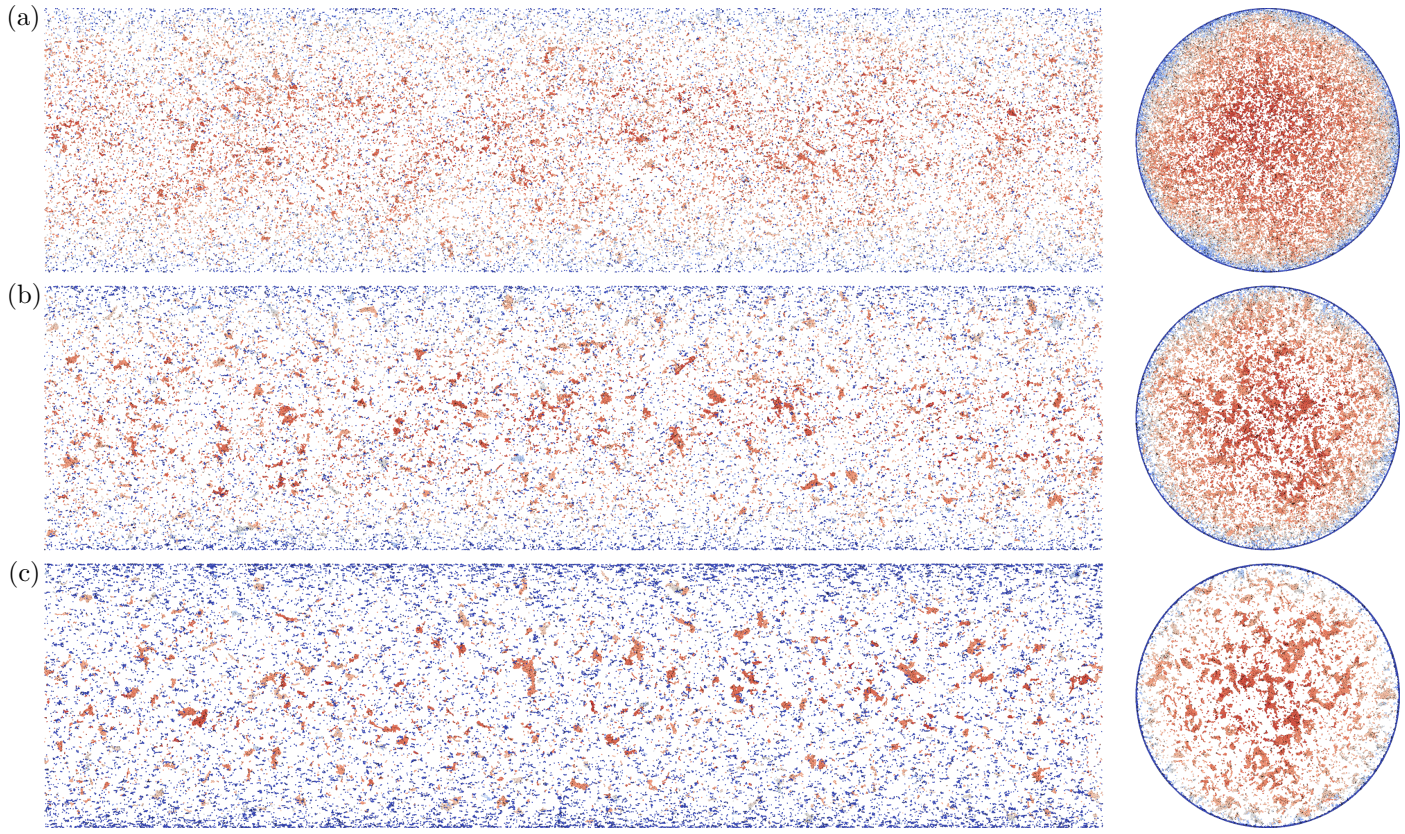

Figure 14: Overview of agglomerating behaviour of particles with $\mathrm{St_e} = 1$ ($\mathrm{St}_\mathcal{L} = 7.3$) with different adhesiveness parameters at time $t^+ = tU/D = 100$: (a) $\mathrm{Ad} = 0.016$; (b) $\mathrm{Ad} = 0.032$; (c) $\mathrm{Ad} = 0.064$. For simulation properties see simulation no. 26, 27 and 28 in table 2 respectively. The particles are coloured according to their instantaneous velocity magnitude. The reader is referred to the online version of this article for a better interpretation.

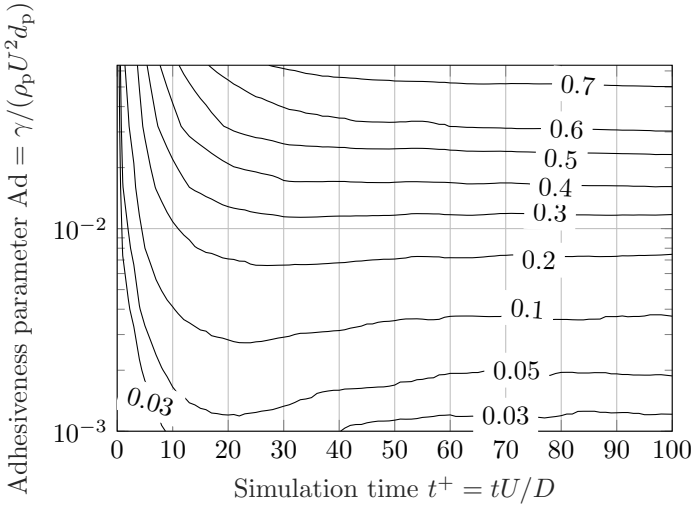

Figure 15: Fraction of particles contained in agglomerates at various adhesiveness parameters as function of simulation time. See simulation no. 29–35 in table 2 for simulation parameters.

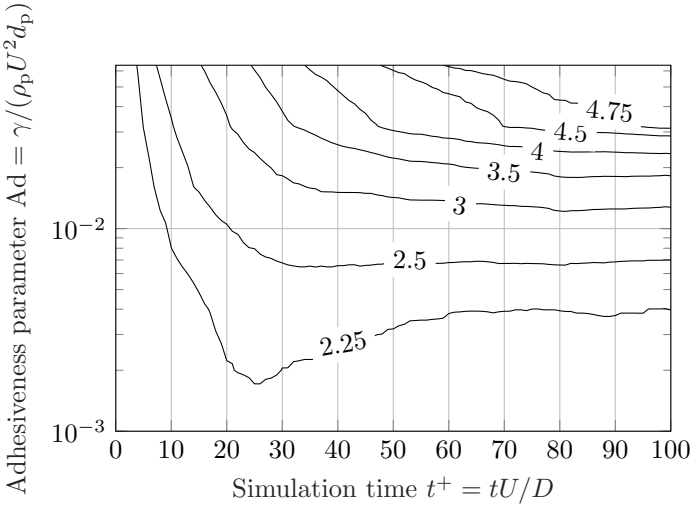

Figure 16: Average number of particles per agglomerate at various adhesiveness parameters $\mathrm{Ad} = \gamma/(\rho_\mathrm{p} U^2 d_\mathrm{p})$ as function of simulation time for particles with $\mathrm{St_e} = 1$ ($\mathrm{St}_\mathcal{L} = 7.3$). See simulation no. 29–35 in table 2 for simulation parameters.

in the different sections of the pipe. Based on the results in figure 17(a) to 17(f), we observe three different regimes. For the weakly adhesive particles with $\mathrm{Ad} = 0.002$ in figure 17(a), the particles tend to collect close to the centre of the pipe with maximum at $0.2 < r/R < 0.3$ without any peak at agglomerate number density at the wall suggesting no particles to deposit at the wall. For intermediate

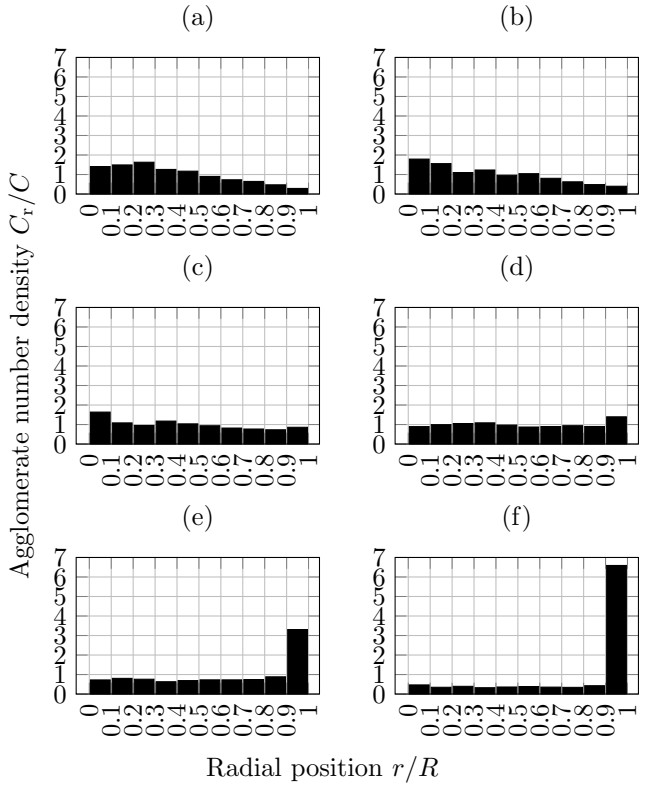

Figure 17: Agglomerate number density in different radial sections of the pipe normalised by the average agglomerate number density in the different radial section of the pipe C_r/C at varying adhesiveness parameter for particles with St = 1 ($St_{\mathcal{L}} = 7.3$) at time $t^+ = tU/D = 100$, see simulation no. 30–35 in table 2 for simulation parameters: (a) Ad = 0.002; (b) Ad = 0.004; (c) Ad = 0.008; (d) Ad = 0.016; (e) Ad = 0.032; (f) Ad = 0.064.

adhesiveness parameters (Ad = 0.016), the agglomerate number density is almost uniform throughout the pipe and for high adhesiveness parameters the is a high number of agglomerates found in the outermost section near the wall where they deposit.

4. Conclusions and discussion

Numerical experiments of how particles agglomerate and deposit in turbulent pipe flows due to van der Waals and electrostatic forces are presented. In this study, we two-way couple Large Eddy Simulations (LES) with the soft-sphere Discrete Element Method (DEM) to fully-resolve the adhesive particle-particle and particle-wall collisions to investigate the early stages of agglomeration and deposition up to $t^+ = 100$.

We report agglomeration and deposition characteristics over a wide range of particle response times and adhesiveness. By varying the Stokes number based on eddy turn over time D/U from $St_e = 0.4$ to $St_e = 25.6$ ($St_{\mathcal{L}} = 2.9$ to $St_{\mathcal{L}} = 185.6$ in terms of integral time scale), the results show how the average particles per agglomerate is highest for particles with an intermediate Stokes number $St_e \approx 6.4$ ($St_{\mathcal{L}} = 46.4$), while the total fraction of particles contained in agglomerates is almost constant up to $St_e \approx 6.4$ ($St_{\mathcal{L}} = 46.4$) after which the fraction of particles in contained in agglomerates decreases rapidly. The results show how more responsive particle $St_e = 0.8$ ($St_{\mathcal{L}} = 5.8$) tend to form agglomerates that are uniformly distributed throughout the flow field with a peak at the wall where particles deposit. At intermediate Stokes numbers $St_e = 6.4$ ($St_{\mathcal{L}} = 46.4$), we observe a distinct increase in agglomerate number density towards the centre of the pipe. For the even less response particles with $St_e = 25.6$ ($St_{\mathcal{L}} = 185.6$) we observe the same behaviour. We attribute this behaviour this behaviour to the Saffman shear lift force, which dominate their radial motion causing less responsive particles and agglomerates to move towards the centre of the pipe.

Last, we report how the transition from almost non-adhesive particles to highly adhesive particles affects the the agglomerating and depositing behaviour. For this purpose, we vary the adhesiveness parameter $Ad = \gamma/(\rho_p U^2 d_p)$ from 0.001 to 0.064. For the less adhesive particles less than 3 % of the particles are contained in agglomerates, while at higher adhesiveness particles more than 70 % of the particles are captured in agglomerates. While varying the adhesiveness of the particles we observe three distinct regimes. For almost non-adhesive particles, agglomerates tend to collect towards the centre of the pipe with a peak at $0.2 < r/R < 0.3$. For particles with intermediate adhesiveness we observe a uniform agglomerate number density through the flow field. For highly adhesive particles, we observe the same almost uniform agglomerate number density throughout the flow field but also a local accumulation of agglomerates being deposited on the wall.

Future studies could focus on later stages of agglomeration and deposition where more or less complex, porous structures form such as the dendritic structures shown in figure 1. To model these later stages of the deposition process more particles would have to be added throughout the simulation.

Acknowledgement

The study is financially sponsored by Innovation Fund Denmark (Grant no. 1305-00036B). Simulations were done by coupling the DEM software LIGGGHTS 3.6.0 (modified to include JKR theory) and the CFD software OpenFOAM 3.0.x using the coupling software CFDEM 3.6.0. Simulations were carried out on the Abacus 2.0 cluster located at the DeIC National HPC Centre, University of Southern Denmark (SDU).

References

[1] P. Saffman, J. Turner, On the collision of drops in turbulent clouds, Journal of Fluid Mechanics 1 (1956) 16–30, DOI: http://doi.org/10.1017/S0022112056000020.

[2] J. Abrahamson, Collision rates of small particles in a vigorously turbulent fluid, Chemical Engineering Science 30 (1975) 1371–1379, DOI: http://doi.org/10.1016/0009-2509(75)85067-6.

[3] C. Meyer, D. Deglon, Particle collision modeling - A review, Minerals Engineering 24 (2011) 719–730, DOI: http://doi.org/10.1016/j.mineng.2011.03.015.

[4] S. Balachandar, J. K. Eaton, Turbulent Dispersed Multiphase Flow, Annual Review of Fluid Mechanics 42 (2010) 111–133, DOI: http://doi.org/10.1146/annurev.fluid.010908.165243.

[5] K. D. Squires, J. K. Eaton, Preferential concentration of particles by turbulence, Physics of Fluids 3 (1991) 1169, DOI: http://doi.org/10.1063/1.858045.

[6] J. Eaton, J. Fessler, Preferential concentration of particles by turbulence, International Journal of Multiphase Flow 20 (1994) 169–209, DOI: http://doi.org/10.1016/0301-9322(94)90072-8.

[7] M. Reeks, The transport of discrete particles in inhomogeneous turbulence, Journal of Aerosol Science 14 (1983) 729–739, DOI: http://doi.org/10.1016/0021-8502(83)90055-1.

[8] A. A. Rao, Flow and segregation behavior of fluidized systems, Ph.D. thesis, University of Florida, 2011.

[9] B. K. Brunk, D. L. Kock, L. W. Lion, Turbulent coagulation of colloidal particles, Journal of Fluid Mechanics 364 (1998) 81–113, DOI: http://doi.org/10.1017/S0022112098001037.

[10] B. K. Brunk, D. L. Kock, L. W. Lion, Observations of coagulation in isotropic turbulence, Journal of Fluid Mechanics 371 (1998) 81–107, DOI: http://doi.org/10.1017/S0022112098002183.

[11] A. Brasil, T. Farias, M.G.Carvalho, U. Koylu, Numerical characterization of the morphology of aggregated particles, Aerosol Science 32 (2001) 489–508, DOI: http://doi.org/10.1016/S0021-8502(00)00097-5.

[12] M. Sommerfeld, S. Stübing, A novel Lagrangian agglomerate structure model, Powder Technology 319 (2017) 34–52, DOI: http://doi.org/10.1016/j.powtec.2017.06.016.

[13] J. Marshall, Particle aggregation and capture by walls in a particulate aerosol channel flow, Aerosol Science 38 (2007) 333–351, DOI: http://doi.org/10.1016/j.jaerosci.2007.01.004.

[14] T. Kobayashi, T. Tanaka, N. Shimada, T. Kawaguchi, DEM–CFD analysis of fluidization behavior of Geldart Group A particles using a dynamic adhesion force model, Powder Technology 248 (2013) 143–152, DOI: http://doi.org/10.1016/j.powtec.2013.02.028.

[15] Y. Gu, A. Ozel, S. Sundaresan, A modified cohesion model for CFD–DEM simulations of fluidization, Powder Technology 296 (2016) 17–28, DOI: http://doi.org/10.1016/j.powtec.2015.09.037.

[16] J. Hærvig, U. Kleinhans, C. Wieland, H. Spliethoff, A. L. Jensen, K. Sørensen, T. J. Condra, On the adhesive JKR contact and rolling models for reduced particle stiffness discrete element simulations, Powder Technology 319 (2017) 472–482, DOI: http://doi.org/10.1016/j.powtec.2017.07.006.

[17] F. D. Dizaji, J. S. Marshall, On the significance of two-way coupling in simulation of turbulent particle agglomeration, Powder Technology 318 (2017) 83–94, DOI: http://doi.org/10.1016/j.powtec.2017.05.027.

[18] S. Ergun, A. A. Orning, Fluid Flow through Randomly Packed Columns and Fluidized Beds, Industrial & Engineering Chemistry 41 (1949) 1179–1184, DOI: http://doi.org/10.1021/ie50474a011.

[19] R. J. Hill, D. L. Koch, A. J. Ladd, The first effects of fluid inertia on flows in ordered and random arrays of spheres, Journal of Fluid Mechanics 448 (2001) 213–241, DOI: http://doi.org/10.1017/S0022112001005948.

[20] R. J. Hill, D. L. Koch, A. J. Ladd, Moderate-Reynolds-number flows in ordered and random arrays of spheres, Journal of Fluid Mechanics 448 (2001) 243–278, DOI: https://doi.org/10.1017/S0022112001005936.

[21] M. Dietzel, M. Sommerfeld, Numerical calculation of flow resistance for agglomerates with different morphology by the Lattice–Boltzmann Method, Powder Technology 250 (2013) 122–137, DOI: http://doi.org/10.1016/j.powtec.2013.09.023.

[22] M. Afkhami, A. Hassanpour, M. Fairweather, D. Njobuenwu, Fully coupled LES-DEM of particle interaction and agglomeration in a turbulent channel flow, Computers and Chemical Engineering 78 (2015) 24–38, DOI: http://doi.org/10.1016/j.compchemeng.2015.04.003.

[23] R. Garg, C. Narayanan, D. Lakehal, S. Subramaniam, Accurate numerical estimation of interphase momentum transfer in Lagrangian–Eulerian simulations of dispersed two-phase flows, International Journal of Multiphase Flow 33 (2007) 1337–1364, DOI: http://doi.org/10.1016/j.ijmultiphaseflow.2007.06.002.

[24] H. Salman, M. Soteriou, Lagrangian simulation of evaporating droplet sprays, Physics of Fluids 16 (2004) 4601, DOI: http://doi.org/10.1063/1.1809132.

[25] J. Capecelatro, O. Desjardins, An Euler–Lagrange strategy for simulating particle-laden flows, Journal of Computational Physics 238 (2013) 1–31, DOI: http://doi.org/10.1016/j.jcp.2012.12.015.

[26] J. Capecelatro, O. Desjardins, R. O. Fox, Numerical study of collisional particle dynamics in cluster-induced turbulence, Journal of Fluid Mechanics 747 (2014) R2, DOI: http://doi.org/10.1017/jfm.2014.194.

[27] J. Zhao, T. Shan, Coupled CFD–DEM simulation of fluid–particle interaction in geomechanics, Powder Technology 239 (2013) 248–258, DOI: http://doi.org/10.1016/j.powtec.2013.02.003.

[28] R. Issa, Solution of the implicitly discretised fluid flow equations by operator-splitting, Journal of Computational Physics 62 (1985) 40–65, DOI: http://doi.org/10.1016/0021-9991(86)90099-9.

[29] F. Nicoud, F. Ducros, Subgrid-Scale Stress Modelling Based on the Square of the Velocity Gradient Tensor, Flow, Turbulence and Combustion 62 (1999) 183–200, DOI: http://doi.org/10.1023/A:1009995426001.

[30] P. Cundall, O. Strack, A discrete numerical model for granular assemblies, Géotechnique 29 (1979) 47–65, DOI: http://doi.org/10.1680/geot.1979.29.1.47.

[31] L. Verlet, Computer "Experiments" on Classical Fluids. I. Thermodynamical Properties of Lennard-Jones Molecules, Physical Review 159 (1967) 98–103, DOI: http://doi.org/10.1103/PhysRev.159.98.

[32] M. Breuer, N. Almohammed, Modeling and simulation of particle agglomeration in turbulent flows using a hard-sphere model with deterministic collision detection and enhanced structure models, International Journal of Multiphase Flow 73 (2015) 171–206, DOI: http://doi.org/10.1016/j.ijmultiphaseflow.2015.03.018.

[33] A. Scurati, D. Feke, I. Manas-Zloczower, Analysis of the kinetics of agglomerate erosion in simple shear flows, Chemical Engineering Science 60 (2005) 6564–6573, DOI: http://doi.org/10.1016/j.ces.2005.05.059.

[34] J. Marshall, Discrete-element modelling of particulate aerosol flows, Journal of Computational Physics 228 (2009) 1541–1561, DOI: http://doi.org/10.1016/j.jcp.2008.10.035.

[35] S. Benyahia, M. Syamlal, T. J. O'Brien, Extension of Hill–Koch–Ladd drag correlation over all ranges of Reynolds number and solids volume fraction, Powder Technology 162 (2006) 166–174, DOI: http://doi.org/10.1016/j.powtec.2005.12.014.

[36] P. Saffman, The lift on a small sphere in a slow shear flow, Journal of Fluid Mechanics 22 (1965) 385–400, DOI: http://doi.org/10.1017/S0022112065000824.

[37] E. Loth, A. Dorgan, An equation of motion for particles of finite Reynolds number and size, Environmental Fluid Mechanics 9 (2009) 187–206, DOI: http://doi.org/10.1007/s10652-009-9123-x.

[38] J. B. McLaughlin, Inertial migration of a small sphere in linear shear flows, Journal of Fluid Mechanics 224 (1991) 261–274, DOI: http://doi.org/10.1017/S0022112091001751.

[39] R. Mei, An approximate expression for the shear lift force on a spherical particle at finite reynolds number, International Journal of Multiphase Flow 18 (1992) 145–147, DOI: http://doi.org/10.1016/0301-9322(92)90012-6.

[40] P. Bagchi, S. Balachandar, Effect of free rotation on the motion of a solid sphere in linear shear flow at moderate Re, Physics of Fluids 14 (2002) 2719, DOI: http://doi.org/10.1063/1.1487378.

[41] K. L. Johnson, K. Kendall, A. D. Roberts, Surface energy and the contact of elastic solids, Proc. R. Soc. Lond. A 324 (1971) 301–313, DOI: http://doi.org/10.1098/rspa.1971.0141.

[42] D. Tabor, Surface forces and surface interactions, Journal of Colloid and Interface Science 58 (1975) 2–13, DOI: http://doi.org/10.1016/0021-9797(77)90366-6.

[43] J. N. Israelachvili, Intermolecular and Surface Forces, Academic Press, 2. edn., iSBN: 978-0-12-375182-9, 1992.

[44] E. J. R. Parteli, J. Schmidt, C. Brümel, K.-E. Wirth, W. Peukert, T. Pöschel, Attractive particle interaction forces and packing density of fine glass powders, Nature Scientific Reports 4 (2014) 1–7, DOI: http://doi.org/10.1038/srep06227.

[45] X. Deng, J. V. Scicolone, R. N. Davé, Discrete element method simulation of cohesive particles mixing under magnetically assisted impaction, Powder Technology 243 (2013) 96–109, DOI: http://doi.org/10.1016/j.powtec.2013.03.043.

[46] C. Thornton, Interparticle sliding in the presence of adhesion, Journal of Physics D: Applied Physics 24 (1991) 1942–1946, DOI: http://doi.org/10.1088/0022-3727/24/11/007.

[47] C. Thornton, K. Yin, Impact of elastic spheres with and without adhesion, Powder Technology 65 (1991) 153–166, DOI: http://doi.org/10.1016/0032-5910(91)80178-L.

[48] M. Oda, J. Konishi, S. Nemat-Nasser, Experimental micromechanical evaluation of strength of granular materials: Effects of particle rolling, Mechanics of Materials 1 (1982) 269–283, DOI: http://doi.org/10.1016/0167-6636(82)90027-8.

[49] K. Iwashita, M. Oda, Rolling Resistance at Contacts in Simulation of Shear Band Development by DEM, Journal of Engineering Mechanics 124 (1998) 285–292, DOI: http://doi.org/10.1061/(ASCE)0733-9399(1998)124:3(285).

[50] C. Dominik, A. Tielens, Resistance to rolling in the adhesive contact of two elastic spheres, Philosophical Magazine A 72 (1995) 783–803, DOI: http://doi.org/10.1080/01418619508243800.

[51] C. Dominik, A. Tielens, The Physics of Dust Coagulation and the Structure of Dust Aggregates in Space, The Astrophysical Journal 480 (1997) 647–673, DOI: http://doi.org/10.1086/303996.

[52] S. Krijt, C. Dominik, A. Tielens, Rolling friction of adhesive microspheres, Journal of Physics D: Applied Physics 47 (2014) 175302 (9pp), DOI: http://doi.org/10.1088/0022-3727/47/17/175302.

[53] P. Gondret, E. Hallouin, M. Lance, L. Petit, Experiments on the motion of a solid sphere toward a wall: From viscous dissipation to elastohydrodynamic bouncing, Physics of Fluids 11 (1999) 2803–2805, DOI: http://doi.org/10.1063/1.870109.

[54] P. Gondret, M. Lance, L. Petit, Bouncing motion of spherical particles in fluids, Physics of Fluids 14 (2002) 643–652, DOI: http://doi.org/10.1063/1.1427920.

[55] D. Legendre, C. Daniel, P. Guiraud, Experimental study of a drop bouncing on a wall in a liquid, Physics of Fluids 17 (2005) 097105, DOI: http://doi.org/10.1063/1.2010527.

[56] S. K. Robinson, Coherent Motions in the Turbulent Boundary Layer, Annual Review of Fluid Mechanics 23 (1991) 601–639, DOI: http://dx.doi.org/10.1146/annurev.fl.23.010191.003125.

[57] J. den Toonder, F. Nieuwstadt, Reynolds number effects in a turbulent pipe flow for low to moderate Re, Physics of Fluids 9 (1997) 3398–3409, DOI: http://doi.org/10.1063/1.869451.

[58] S. B. Pope, Ten questions concerning the large-eddy simulations of turbulent flows, New Journal of Physics 6 (2004) 35, DOI: http://doi.org/10.1088/1367-2630/6/1/035.

[59] M. Quadrio, P. Luchini, Integral space-time scales in turbulence wall flows, Physics of Fluids 15 (2003) 2219–2227, DOI: http://doi.org/10.1063/1.1586273.

[60] V. Armenio, U. Piomelli, V. Fiorotto, Effect of the subgrid scales on particle motion, Physics of Fluids 11 (1999) 3030–3042, DOI: http://doi.org/10.1063/1.870162.

[61] L. Zhao, C. Marchioli, H. Andersson, Stokes number effects on particle slip velocity in wall-bounded turbulence and implications for dispersion models, Physics of Fluids 24 (2012) 021705, DOI: http://doi.org/10.1063/1.3690071.

Nomenclature

$\mathrm{Ad} = \gamma/(\rho_\mathrm{p} U^2 d_\mathrm{p})$	Adhesiveness parameter	-
C	Agglomerate number density	$1/\mathrm{m}^3$
$\mathrm{Fr} = U/\sqrt{g_\mathrm{r} d_\mathrm{p}}$	Froude number	-
D	Pipe diameter	m
d_p	Particle diameter	m
$g_\mathrm{r} = (1 - 1/\chi)g$	Buoyancy corrected gravity	$\mathrm{m/s}^2$
$\mathrm{Kn} = \lambda/d_\mathrm{p}$	Knudsen number	-
L	Length of periodic pipe section	m
n	Number	
p	Pressure	Pa
R	Effective particle radius	m
R	Pipe radius	m
r	Particle radius	m
r	Radial coordinate	m
s	Time lag	s
t	Time	s
$t^+ = tU/D$	Dimensionless time	-
U	Fluid bulk velocity	m/s
V	Cell volume	m^3
$\mathrm{Re} = UD/\nu$	Reynolds number	-
$\mathrm{St}_\mathrm{e} = \tau_\mathrm{p}/\tau_\mathrm{e}$	Eddy turn-over time Stokes number	-
$\mathrm{St}_\mathcal{L} = \tau_\mathrm{p}/\tau_\mathcal{L}$	Turbulence integral time scale Stokes number	-
Greek letters		
δ	Kroneckers delta	-
δt	Time step size	s
Δ	Cell length	m
$\Delta\gamma/\gamma$	Adhesion hysteresis parameter	-
$\epsilon = d_\mathrm{p}/D$	Dimensionless particle diameter	-
$\lambda = E/(\rho_\mathrm{p} U^2)$	Elasticity parameter	-
λ	Mean free molecular path	m
μ	Dynamic viscosity	kg/(m·s)
ρ	Density	$\mathrm{kg/m}^3$
$\rho(s)$	Normalised auto-correlation coefficient	-
τ	Response time	s
ϕ	Particle volume fraction	-
$\chi = \rho_\mathrm{p}/\rho_\mathrm{f}$	Density ratio	-

Subscripts

agg	Agglomerate
f	Fluid
i,j	particle indices
mod	Stiffness-modified values
p	Particle
x, y, z	Spatial coordinates

Superscripts

$-$	Filtered values
$+$	Viscous units

Acronyms

sgs	Sub-grid scale
CFD	Computational Fluid Dynamics
DEM	Discrete Element Method
DNS	Direct Numerical Simulation
LES	Large Eddy Simulation
WALE	Wall-Adapting Local Eddy-viscosity